TU Delft

Delft University of Technology

Instabilities and cavitation in cylindrical wavy line contact

A Maugis analysis

Van Dokkum, Jan Steven; Pérez-Ràfols, Francesc; Nicola, Lucia

DOI
10.1016/j.ijsolstr.2024.113008

Publication date
2024

Document Version
Final published version

Published in
International Journal of Solids and Structures

Citation (APA)
Van Dokkum, J. S., Pérez-Ràfols, F., & Nicola, L. (2024). Instabilities and cavitation in cylindrical wavy line contact: A Maugis analysis. *International Journal of Solids and Structures*, *305*, Article 113008. https://doi.org/10.1016/j.ijsolstr.2024.113008

Important note
To cite this publication, please use the final published version (if applicable).
Please check the document version above.

Copyright
Other than for strictly personal use, it is not permitted to download, forward or distribute the text or part of it, without the consent of the author(s) and/or copyright holder(s), unless the work is under an open content license such as Creative Commons.

Takedown policy
Please contact us and provide details if you believe this document breaches copyrights.
We will remove access to the work immediately and investigate your claim.

This work is downloaded from Delft University of Technology.
For technical reasons the number of authors shown on this cover page is limited to a maximum of 10.

Green Open Access added to TU Delft Institutional Repository

'You share, we take care!' - Taverne project

https://www.openaccess.nl/en/you-share-we-take-care

Otherwise as indicated in the copyright section: the publisher is the copyright holder of this work and the author uses the Dutch legislation to make this work public.

International Journal of Solids and Structures 305 (2024) 113008

Contents lists available at ScienceDirect

International Journal of Solids and Structures

journal homepage: www.elsevier.com/locate/ijsolstr

Instabilities and cavitation in cylindrical wavy line contact: A Maugis analysis

Jan Steven Van Dokkum [a,b], Francesc Pérez-Ràfols [c], Lucia Nicola [d,*]

[a] Materials Science and Engineering, Delft University of Technology, Delft, The Netherlands
[b] Institute for Building Materials, ETH Zurich, Zurich, Switzerland
[c] Serra Hunter Fellow at Universitat Politècnica de Catalunya, EPSEM, Manresa, Spain
[d] Department of Industrial Engineering, University of Padova, Padua, Italy

ARTICLE INFO

Keywords:
Contact
Adhesion
Cylinder
Analytical solutions

ABSTRACT

The Maugis analysis is applied to adhesive contact between a cylinder with various wave profiles and a semi-infinite, elastic half-plane. We extend the analysis of Waters, Lee and Guduru, who consider the adhesive contact of a Hertzian indenter on a semi-infinite, elastic half-space with axi-symmetric, wave profiles. This work gives the closed-form contact mechanical solution for continuous, line contact without the need for any approximation. The resulting semi-analytical model serves to complement existing (numerical) models of adhesive line contact with the static load-area response as a reference. Herewith we analyse adhesion-induced loading-unloading hysteresis and contrast semi-analytical and numerical result to assess the limit of the former analysis. We confirm that roughness-induced dissipation vanishes with increasing wave roughness and decreasing Maugis parameter due to an increase in the range of adhesion and cavitation. Instability and cavitation are mutually exclusive at a given load-area locus yet occur successively in the same contact. An interesting result is that the Johnson parameter, that is known to govern the amplification of adhesion in the JKR-limit, bounds the load-area envelope irrespective of Maugis parameter. However, the Johnson parameter does not control the occurrence of roughness-induced dissipation and thus interface toughening.

1. Introduction

The current push towards tunable adhesion has given rise to a renewed interest in the contact mechanics of adhesives. Recent applications of tunable adhesion exploit its directional (Hwang et al., 2023), force (Linghu et al., 2023) and texture (Badler et al., 2023) dependence. As adhesion becomes dominant when the scale of contacting bodies decreases, the omnipresent surface roughness plays an increasingly large role (Waters et al., 2009). Small scale roughness is known to increase the pull-off force in soft matter (Briggs and Briscoe, 1977). Microscale asperities snapping into or out of contact toughen the interface as well (Guduru and Bull, 2007). More recently, Sanner and Pastewka (2022), Sanner et al. (2024) show that pinning of the contact perimeter retards both its advancement when coming into contact and its retraction when pulling away for randomly rough contacts with near-circular contact area. Most recently, the importance of dissipative processes that occur at a distance from the interface in soft matter contact is recognised (Müser and Nicola, 2022). The observable adhesion depends not only on material properties, loading history, direction and rate, but also on multi-scale roughness (Creton and Leibler, 1996; Persson and Scaraggi, 2014; Dalvi et al., 2019; Wang and Müser, 2023). One method of capturing these dependencies is to study rough surface contact mechanics using elementary body and surface geometries (Waters et al., 2009).

The contact mechanics of smooth, adhesive axi-symmetric contact has been well-understood for over three decades now. The load-area and load–displacement response are governed by the Tabor parameter (Tabor, 1977), which controls the transition from rigid-body to JKR behaviour (Maugis, 1992; Johnson and Greenwood, 1997). Similarly, axi-symmetric contact with wave profile is studied analytically and experimentally by Guduru (Guduru, 2007; Guduru and Bull, 2007), and extended to a cohesive zone model by Waters et al. (2009). Guduru (2007) and Guduru and Bull (2007) show that waviness introduces instabilities that dissipate mechanical energy; adhesive dissipation and the pull-off force both increase with waviness, provided contact is compliant. Waters et al. (2009) theorise that adhesion enhancement by dissipation depends on the Maugis parameter (Maugis, 1992), that controls the rigid-to-compliant transition of the contact. The values of the Tabor and Maugis parameter depend on the cohesive zone models (Lennard-Jones, 1931; Dugdale, 1960; Barthel, 1998) and are proportional (Tabor, 1977; Maugis, 1992). The proportionality in *e.g.* Maugis (1992), Johnson and Greenwood (1997), Zheng and Yu (2007) and Zhu et al. (2021, 2022) depends on the choice one makes

* Corresponding author.
E-mail address: lucia.nicola@unipd.it (L. Nicola).

https://doi.org/10.1016/j.ijsolstr.2024.113008
Received 1 March 2024; Received in revised form 8 July 2024; Accepted 31 July 2024
Available online 8 August 2024
0020-7683/© 2024 Elsevier Ltd. All rights are reserved, including those for text and data mining, AI training, and similar technologies.

on the equivalence between the adhesive traction in the Lennard-Jones (1931) and Dugdale (1960) model.

Research into the contact mechanics of adhesive line contact, that is simpler than surface contact, starts a decade later. There are three notable reasons for more interest in axi-symmetric than line contact, namely: experimental convenience, because problems of orientation and alignment are avoided (Johnson and Greenwood, 2008); the contact area and indentation are the observable quantities (Johnson and Johnson, 1987; Barber, 2018); and, the availability of a well-documented set of integral relations between the load, the indentation and the contact area (Maugis, 2000). Nonetheless, also line contact has its own merits, namely: studying a moving contact is practicable with rolling cylinders (She et al., 1998; She and Chaudhury, 2000); and, it is representative for the many engineering materials that display anisotropic roughness after polishing (Carbone and Pierro, 2012). Baney and Hui (1997), and Johnson and Greenwood (2008) are the first to apply the Maugis analysis (Maugis, 1992, 2000) to smooth cylindrical, line contact. The load-area relationship in the JKR-limit of a cylinder with a wave profile is presented by Guduru (2007). Other notable Maugis analyses are those of infinite, sinusoidal profiles (Jin et al., 2016), and (periodic) slit(s) (Chumak et al., 2014; Chumak, 2016). The works (Johnson and Greenwood, 2008; Chumak et al., 2014; Chumak, 2016; Jin et al., 2016) show that also for line contact the load-area response is governed by the Maugis parameter (Baney and Hui, 1997). However, unlike smooth (Baney and Hui, 1997; Johnson and Greenwood, 2008) and elementary (periodic) profiles (Jin et al., 2016; Chumak et al., 2014; Chumak, 2016), wavy line contact in Guduru (2007) is not extended to an exact Maugis analysis yet.

Continuous intimate contact is pre-requisite to the (Maugis) analysis (Maugis, 1992, 2000); the predictions in Baney and Hui (1997), Guduru (2007), Johnson and Greenwood (2008), Waters et al. (2009), Chumak et al. (2014), Chumak (2016), Jin et al. (2016) and Sanner and Pastewka (2022) are only valid when surfaces/profiles come into continuous intimate contact. Most recently, Zhu et al. (2021) show that adhesive dissipation and the pull-off force decrease with Maugis parameter in sphere-axisymmetric wavy surface contact (Guduru, 2007), and report an increased chance of cavitation with roughness. They (Zhu et al., 2021) define "*cavitation*" as the appearance of a toroidal gap(s) under tensile traction surrounded by intimate contact on either side. The intimate contact can thus be discontinuous and the Maugis analysis (Waters et al., 2009) cannot be applied. Numerical boundary-element methods (Campaná and Müser, 2007; Bazrafshan et al., 2017) find quasi-static, stable contact and fully self-consistent models (Attard and Parker, 1992; Greenwood, 1997; Feng, 2000; Zhu et al., 2021) static contact also when cavitation occurs. Hence the validity of Maugis analyses has to be checked with numerical result. Wherefore we highlight when cavitation occurs in line contact.

The influence of roughness on adhesion-induced hysteresis is captured by the Johnson parameter (Kesari et al., 2010), a geometrical parameter that depends on the wave amplitude and length. It is well known that the pull-off force increases with wave roughness for large Maugis parameters (Maugis, 1992). The validity of the Johnson parameter is limited to waviness parameters where the asymptotic expansion by Kesari et al. (2010) and Ciavarella (2016) holds, *i.e.* for large contact areas and/or small wavelengths. The Johnson parameter is a measure of the load-area envelope in wavy line contact (Jin et al., 2016; Pérez-Ràfols et al., 2023) as well. Moreover, as the static equilibrium path included in the envelope is wavy it cannot be followed during approach and detachment, and there are unstable jumps to the next-closest stable equilibrium (Guduru, 2007; Guduru and Bull, 2007; Sanner and Pastewka, 2022). These instabilities dissipate potential energy and cause toughening of the interface. In axi-symmetric contact the Johnson parameter for single sinusoidal contact scales the energy loss per loading-unloading cycle (Kesari et al., 2010; Kesari and Lew, 2011). The Johnson parameter is also a measure of roughness-induced dissipation while the Maugis parameter has to be sufficiently large so that the JKR-limit is approached. Whether the Johnson parameter is a measure of the load-area envelope and roughness-induced dissipation also for small Maugis parameters, for which there is a departure from the JKR-limit, is currently unclear (Ciavarella, 2016). This we investigate for line contact herein.

The difference between instabilities and cavitation is that the former is a dissipation mechanism that toughens the interface, while we show that the latter is not. Zhu et al. (2021) state that contact weakens because cohesive strength decreases with Maugis parameter, and that the chance of cavitation increases with roughness. Furthermore, they (Zhu et al., 2021) observe cavitation in the detachment process for large roughness and finite Maugis parameter, demonstrating that Guduru's assumption (Guduru, 2007) on continuous contact does not hold after the contact is pressed sufficiently. The toughness of wavy axi-symmetric contact thus depends on the Maugis parameter as well. Any observation on axi-symmetric contact does not necessary hold in line contact (Baney and Hui, 1997; Johnson and Greenwood, 2008) though. Hence it is to be established whether observations in Waters et al. (2009), Kesari et al. (2010), Kesari and Lew (2011), Ciavarella (2016) and Zhu et al. (2021) also hold for adhesive, line contact, as this is currently unknown.

Herein, we study two-scale roughness by combining the Maugis analysis for cylindrical contact (Baney and Hui, 1997; Maugis, 2000) with wavy surface adhesion in plane strain (Waters et al., 2009). To simplify the problem, roughness is modelled as a single-wavelength wave superimposed on the profile of a rigid, infinite cylinder in contact with a semi-infinite half-plane. Hence we remedy the lack of a Maugis analysis of rough, line contacts. For two Johnson parameters, we track the load and contact area with various wave amplitudes (or wavelengths), and vary the range of adhesion between adhesionless and JKR-type adhesion. This permits us to establish whether and/or when the Johnson parameter controls adhesion and roughness-induced dissipation towards adhesionless line contact. Wherefore we compare the semi-analytical with boundary-element method (Van Dokkum and Nicola, 2019) result, which also delimits the validity of our Maugis analysis.

2. Problem statement

We consider the frictionless, adhesive contact of a rigid, infinite cylinder with a wave profile in contact with an isotropic, linear elastic solid. The cylinder profile

$$f(x) = C - \frac{x^2}{2R} - A\left(1 - \cos\left(\frac{2\pi x}{\zeta}\right)\right), \tag{1}$$

where x is the horizontal distance from the centreline of the cylinder, R is the cylindrical radius, and A and ζ the amplitude and the wavelength of the roughness, respectively. The constant C depends on the location of the coordinate origin of the cylinder profile. In Fig. 1, we give a schematic representation of the problem considered herein. In frictionless, symmetric continuous contact, the gradient of the surface displacement (Sneddon, 1965):

$$\frac{\partial f}{\partial x} \equiv \frac{\partial u}{\partial x} = \frac{2}{\pi E^*}\int_{-a}^{a} \frac{p(\xi)}{x-\xi}\,\mathrm{d}\xi, \quad \text{for,} \quad -a < x < a, \tag{2}$$

where $p(x)$ is the traction and $E^* \equiv E/\left(1-\nu^2\right)$ the effective modulus, with the isotropic, linear elastic modulus E and Poisson's ratio ν. The intimate contact area a is defined as the area with zero gap, *i.e.* $g(|x| \le a) = 0$. We use the Dugdale-Maugis model (Dugdale, 1960; Maugis, 1992) to describe the adhesive interaction between the rigid indenter and the elastic substrate with a constant work of adhesion $\Delta\gamma$. The traction $p(a < |x|) = \sigma$ is a positive constant whenever the gap between the indenter and the elastic substrate $g(a < |x|)$ is

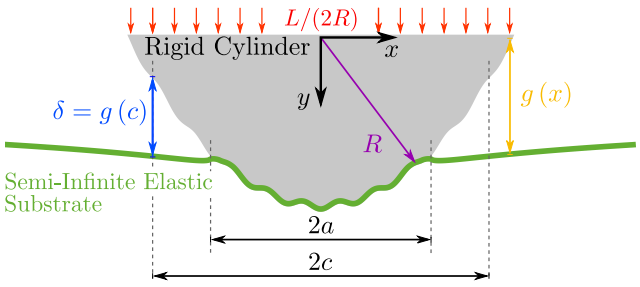

Fig. 1. Schematic representation of a rigid indenter with radius R in intimate contact with a semi-infinite, elastic substrate for an applied load L, with gap $g(x)$, intimate contact area a, adhesive strip $|c-a|$ and interaction length δ, that controls adhesion.

positive but smaller than the interaction length $\delta \equiv \Delta\gamma/\sigma$. We solve a mixed-boundary value problem, namely:

$$\begin{array}{lll} g(|x| \le a) = 0, & p(|x| \le a) < \sigma, & \text{intimate contact;} \\ 0 < g(a < |x| \le c) < \delta, & p(a < |x| \le c) = \sigma, & \text{adhesive strip;} \\ \delta \le g(c < |x|), & p(c < |x|) = 0, & \text{out of contact;} \end{array} \quad , \tag{3a}$$

with the absolute value $|\bullet|$ of scalar $\bullet$, the total traction,

$$p(x) = p^{\mathrm{c}}(x) + p^{\mathrm{a}}(x), \tag{3b}$$

and the gap,

$$g(x) \equiv f(x) - u(x), \tag{3c}$$

where $u(x)$ is displacement of the substrate, $p^{\mathrm{c}}(x)$ and $p^{\mathrm{a}}(x)$ the adhesionless and adhesive traction, respectively, and $|c-a|$ the size of the adhesive strip. The total substrate displacement

$$u(x) = u_{\mathrm{H}}(x) + u_{\mathrm{w}}(x) + u_{\mathrm{a}}(x) + C, \tag{4}$$

where the first and second term on the right-hand-side (RHS) are the displacements due to frictionless, adhesionless continuous (Hertzian) cylindrical contact (Baney and Hui, 1997; Johnson and Greenwood, 2008) and the wave roughness, respectively; and, the third term on the RHS is due to the adhesive traction $p^{\mathrm{a}}(|x| \le c)$. The size of this adhesive strip $|c-a|$ is determined such that the stress singularity at the edges of intimate adhesive contact, $|x| = c$, is cancelled (Barenblatt, 1962) by the constant adhesive traction $p^{\mathrm{a}}(a < |x| \le c) \equiv \sigma$ (Maugis, 1992, 2000).

According to the Maugis analysis (Maugis, 1992, 2000) in adhesive elastic Hertzian contact, traction and displacement are the sum of the Hertzian $u_{\mathrm{H}}(x)$ and $p^{\mathrm{H}}(x)$, and adhesive contributions $u_{\mathrm{a}}(x)$ and $p^{\mathrm{a}}(x)$. The adhesive traction $p^{\mathrm{a}}(x)$ and displacement $u_{\mathrm{a}}(x)$ due to symmetric, adhesive line contact are presented by Baney and Hui (1997), and Johnson and Greenwood (2008), and apply to any symmetric and continuous, adhesive line contact that makes use of the Dugdale-Maugis model (Dugdale, 1960; Maugis, 1992). We summarise the main result of Baney and Hui (1997) and Johnson and Greenwood (2008) in Appendix A. Guduru (2007) added an adhesionless traction, $p^{\mathrm{w}}(x)$, due to the presence of the wave profile $u_{\mathrm{w}}(|x| \le a)$ in intimate contact, yet limits the result to an infinitesimal range of adhesion, *i.e.* $c \equiv a$. We revisit Guduru's (Guduru, 2007) derivation of, and firstly rewrite the expression for, the adhesionless traction $p^{\mathrm{c}}(x) = p^{\mathrm{H}}(x) + p^{\mathrm{w}}(x)$. Subsequently, we derive, for the first time, the wave displacement $u_{\mathrm{w}}(x)$ caused by adhesionless, wavy traction $p^{\mathrm{w}}(x)$ in line contact. Finally, we present the load-area response for generic roughness parameters $\{A/R, R/\zeta\}$ with a finite range of adhesion, *i.e.* $0 \lesssim \delta \lesssim \infty$.

3. Maugis analysis

3.1. Adhesionless traction

Equation (2) is a Cauchy-type singular integral equation, which is solved as in Barber (2018). The profile $f(x)$ and adhesionless traction $p^{\mathrm{c}}(\xi)$ are expressed as Fourier series:

$$\frac{\partial}{\partial\phi} f(\phi) = \sum_{n=1}^{\infty} f_n \sin(n\phi), \tag{5a}$$

and,

$$p^{\mathrm{c}}(\theta) = \sum_{n=0}^{\infty} p_n^{\mathrm{c}} \frac{\cos(n\theta)}{\sin(\theta)}; \tag{5b}$$

with a change of variables,

$$x = a\cos(\phi); \quad \text{and,} \quad \xi = a\cos(\theta), \tag{5c}$$

where p_n^{c} and f_n are the discrete Fourier transform coefficients of the wavenumber n. Substituting the adhesionless traction (5b) and coordinates (5c) in Eq. (2) and solving the integral by means of contour integration, Guduru (2007) reproduces the pressure

$$\frac{E^*}{2a}\frac{\partial}{\partial\phi} f(\phi) = \sum_{n=1}^{\infty} p_n^{\mathrm{c}} \int_0^{\pi} \frac{\sin(\phi)\cos(n\theta)}{\cos(\theta) - \cos(\phi)}\,\mathrm{d}\theta = \sum_{n=1}^{\infty} p_n^{\mathrm{c}} \sin(n\phi), \tag{6}$$

We present the full derivation by Guduru (2007) of the adhesionless traction $p^{\mathrm{c}}(x)$ in Appendix B. We simplify the equation (65) for the adhesionless traction in Guduru (2007) to

$$p^{\mathrm{c}}(\theta) = -\frac{E^* a \sin(\theta)}{2R} - \frac{\pi E^* A \sin(\theta)}{\zeta} \int_0^{\frac{2\pi a}{\zeta}} \mathrm{J}_0(t) \cos\left(\left(t - \frac{2\pi a}{\zeta}\right)\cos(\theta)\right)\mathrm{d}t, \tag{7}$$

with the zeroth-order Bessel function $\mathrm{J}_0(t)$ (B.10). Noting that when the amplitude $A = 0$, and/or the wavelength $\zeta \sim 0$ and ∞, and using Eq. (5c), we reduce the traction (7) to that of adhesionless cylindrical contact $p^{\mathrm{H}}(x)$ (Barber, 2018). We prefer the integral expression of the adhesionless traction due to wave roughness in the second term on the RHS of Eq. (7). The wave deformation gradient $\partial u_{\mathrm{w}}/\partial x$ then becomes a definite, double integral that we can and will solve in the following.

3.2. Adhesionless substrate deformation

The total substrate deformation in the absence of adhesion

$$u_{\mathrm{H}}(x) + u_{\mathrm{w}}(x) = \int \frac{\partial u_{\mathrm{H}}}{\partial x}\,\mathrm{d}x + \int \frac{\partial u_{\mathrm{w}}}{\partial x}\,\mathrm{d}x + C, \tag{8}$$

where the first and second term, on the RHS and left-hand-side (LHS), are the substrate deformation due to the Hertzian cylinder and the wave profile, respectively. The deformation gradient $\partial u/\partial x$ outside of intimate contact $a < |x|$ is given by Eq. (2). Substituting the adhesionless traction (7) in the deformation gradient (2), and rewriting the spatial coordinate $x = a/\cos(\phi)$, we solve the deformation gradient due to the cylindrical contact $\partial u_{\mathrm{H}}/\partial x$, and the waviness $\partial u_{\mathrm{w}}/\partial x$ separately making use of the sum rule (Abramowitz et al., 1988). The former is done herein for illustrative purpose of the contour integral method C that we employ in the following.

We obtain the integral on the RHS of Eq. (2) for the first (Hertzian) term on the RHS of Eq. (7) by means of contour integration in Appendix C.1. Substituting the spatial coordinate x in the integral (C.29), we simplify the resultant Hertzian deformation gradient to

$$\frac{\partial}{\partial x} u_{\mathrm{H}}(x) = \frac{x}{R} - \frac{\sqrt{x^2 - a^2}}{R}, \qquad \text{for,} \qquad a < |x|. \tag{9}$$

This equation (9) is the well-known result that one finds in *e.g.* the compendia by Johnson and Johnson (1987) and Barber (2018). The Hertzian substrate deformation

$$u_{\mathrm{H}}(x) = \frac{x^2}{2R} - \frac{x}{2R}\sqrt{x^2 - a^2} + \frac{a^2}{2R}\cosh^{-1}\left(\frac{x}{a}\right), \tag{10}$$

that we obtain by integrating Eq. (9) and a change of variables (Barber, 2018). Substituting the second (wave) term on the RHS of the adhesionless traction (7) in the deformation gradient (2), we present the wave deformation gradient as

$$\frac{\partial}{\partial x}u_{\mathrm{w}}(x) = \frac{A}{\zeta}\int_0^{\frac{2\pi a}{\zeta}} J_0(t)\int_0^{2\pi}\frac{\cos(\phi)\sin^2(\theta)}{1-\cos(\theta)\cos(\phi)}\cos\left(\left(t-\frac{2\pi a}{\zeta}\right)\cos(\theta)\right)\mathrm{d}\theta\,\mathrm{d}t. \tag{11a}$$

We obtain the double integral on the RHS of Eq. (11a) by means of contour integration in Appendix C.2. Using the inner integral (C.37) and substituting the outer integral (C.39a) in Eq. (11a), we find the wave deformation gradient

$$\frac{\partial}{\partial x}u_{\mathrm{w}}(x) = \left(\frac{\pi a}{\zeta}\right)^2\frac{2A}{x}\sum_{k=0}^{\infty}\frac{1}{\Gamma(k+1)\Gamma(k+2)}\frac{(-1)^k}{1+2k}\left(\frac{\pi a}{\zeta}\right)^{2k}\cdots \tag{11b}$$
$$\cdots\ {}_1\mathrm{F}_2\left(\frac{1}{2};k+1,k+\frac{3}{2};-\left(\frac{\pi a}{\zeta}\right)^2\right){}_2\mathrm{F}_1\left(1,k+\frac{1}{2};k+2;\left(\frac{a}{x}\right)^2\right),$$

where $\Gamma(\bullet_1)$ is the Gamma function (Abramowitz et al., 1988), ${}_2\mathrm{F}_1(\bullet_2,\bullet_3;\bullet_4;z)$ is the hypergeometric function (C.35b) and ${}_1\mathrm{F}_2(\bullet_5,\bullet_6;\bullet_7;z)$ the generalised hypergeometric function (C.39b), with scalars $\bullet_{(1,\dots,7)}$. Solving the second integral on the RHS of Eq. (8) in Appendix D, substituting the integral (D.41a) in Eq. (D.40), and noting that the substrate deformation is real-valued, we find the wave displacement

$$u_{\mathrm{w}}(x) = \frac{A}{\sqrt{\pi}}\left(\frac{\pi a}{\lambda}\right)^2\sum_{k=0}^{\infty}\frac{(-1)^{3k}}{\Gamma(2k+2)}\left(\frac{2\pi a}{\zeta}\right)^{2k}\cdots \tag{12}$$
$$\cdots\ {}_1\mathrm{F}_2\left(\frac{1}{2};k+1,k+\frac{3}{2};-\left(\frac{\pi a}{\zeta}\right)^2\right)\Re\left(\mathrm{G}^{2,2}_{3,3}\left(-\left(\frac{a}{x}\right)^2\middle|\begin{matrix}0,\frac{1}{2}-k,1\\0,0,-k-1\end{matrix}\right)\right),$$

where $\Re(\bullet_1)$ is the real part of the complex scalar $\bullet_1$ and $\mathrm{G}^{l,0}_{i,j}(\bullet_2)$ the Meijer-G function (D.41b). Substituting the substrate deformations (10) and (12) back into Eq. (8) and taking the central crest of the rigid punch as the origin $\{x,y\}=\{0,0\}$, we find that the integration constant vanishes, and use $C=0$ in the total substrate displacement (4) as well.

3.3. Load-area response

In the following, we use the normalisation:

$$A = \alpha\sqrt[3]{\frac{\Delta\gamma^2 R}{(E^*)^2}};\quad \zeta = \beta\sqrt[3]{\frac{\Delta\gamma^2 R}{(E^*)^2}};\quad \sqrt{\frac{2\Delta\gamma\zeta}{\pi^2A^2E^*}} = \sqrt{\frac{2\beta}{\pi^2\alpha^2}}; \tag{13a}$$
$$a = \bar{a}\sqrt[3]{\frac{\Delta\gamma R^2}{E^*}};\quad L = \bar{L}\sqrt[3]{E^*\Delta\gamma^2 R};\quad x = \bar{x}\sqrt[3]{\frac{\Delta\gamma^2 R}{(E^*)^2}};\quad u = \bar{u}\sqrt[3]{\frac{\Delta\gamma^2 R}{(E^*)^2}};$$
$$g = \bar{g}\sqrt[3]{\frac{\Delta\gamma^2 R}{(E^*)^2}};\quad \delta = \bar{\delta}\sqrt[3]{\frac{\Delta\gamma^2 R}{(E^*)^2}};\quad \text{and,}\quad p = \bar{p}\sigma = \bar{p}\lambda\sqrt[3]{\frac{(E^*)^2\,\Delta\gamma}{R}},$$

where α and β are the normalised wave amplitude and wavelength, respectively, $\sqrt{\beta/\alpha^2}$ the scaled Johnson parameter (Johnson, 1995), $\bar{a}$ the normalised intimate contact area, $\bar{L}$ the normalised total load, $\bar{x}$ the normalised x-coordinate, $\bar{u}$ the normalised displacement, $\bar{g}$ the normalised gap, $\bar{\delta}$ the normalised interaction range and $\bar{p}$ the normalised traction. The Maugis parameter λ is a dimensionless parameter that governs the transition from rigid cylindrical behaviour, $\lambda < 1/4$, to JKR behaviour, $3 < \lambda$, in which pull-off occurs discontinuously from a finite contact area (Johnson and Greenwood, 2008). Note that our notation of the Johnson parameter $\sqrt{2\beta/(\pi\alpha)^2}$ differs with *e.g.* the symbol "α" in Johnson (1995), Kesari et al. (2010), Ciavarella (2016) and Pérez-Ràfols et al. (2023). The ratio of the adhesive strip,

$$m \equiv \frac{c}{a}, \tag{13b}$$

where we follow the notations for the integer index m by Guduru (2007) before; and, in the following, the ratio m, by *e.g.* Baney and Hui (1997), Johnson and Greenwood (2008), and Waters et al. (2009). The total normalised load

$$\bar{L}_{\mathrm{M}} = \bar{L}_{\mathrm{c}}(\bar{a}) + \bar{L}^{\mathrm{M}}_{\mathrm{a}}(\bar{a}) = \frac{\pi\bar{a}^2}{4} - 2\lambda\bar{a}\sqrt{m^2-1} + \frac{\pi^2\alpha\bar{a}}{\beta}\mathrm{J}_1\left(\frac{2\pi\bar{a}}{\beta}\right). \tag{14}$$

where $L_{\mathrm{c}}(a)$ is the adhesionless load (B.13) and $L^{\mathrm{M}}_{\mathrm{a}}(a)$ the adhesive load (A.4c). Substituting Eqs. (A.5b), (10) and (12) in the definition of the gap at the edges of contact

$$g(|x|=c) \equiv \delta, \tag{15a}$$

we give this normalised gap as,

$$1 = \frac{4}{\pi}\lambda^2\bar{a}\left(\sqrt{m^2-1}\cosh^{-1}(m) - m\ln(m)\right) + \frac{1}{2}\lambda\bar{a}\left(m\sqrt{m^2-1} - \cosh^{-1}(m)\right)\cdots \tag{15b}$$
$$\cdots\quad -2\alpha\lambda\sin^2\left(\frac{\pi m\bar{a}}{\beta}\right) + \frac{\alpha\lambda}{\sqrt{\pi}}\left(\frac{\pi\bar{a}}{\beta}\right)^2\sum_{k=0}^{\infty}\frac{(-1)^{3k}}{\Gamma(2k+2)}\left(\frac{2\pi\bar{a}}{\beta}\right)^{2k}\cdots$$
$$\cdots\ {}_1\mathrm{F}_2\left(\frac{1}{2};k+1,k+\frac{3}{2};-\left(\frac{\pi\bar{a}}{\beta}\right)^2\right)\Re\left(\mathrm{G}^{2,2}_{3,3}\left(-\left(\frac{1}{m}\right)^2\middle|\begin{matrix}0,\frac{1}{2}-k,1\\0,0,-k-1\end{matrix}\right)\right).$$

Finally, the size of the adhesive strip m is obtained numerically by approximating the infinite series on the RHS of Eq. (15b) with $k=0,\dots,k_{\max}$ terms of the same sum, because no closed-form analytical solution is found. Closed-form analytical solutions do exist in the JKR (Johnson et al., 1971) and M-DMT (Maugis, 1992; Greenwood, 2022) limit, which we summarise in Appendix E and outline in Fig. 2.

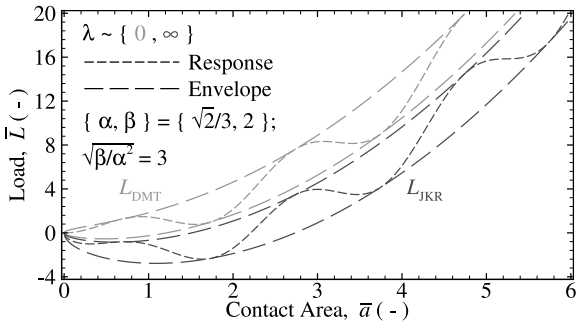

Fig. 2. Normalised load $\bar{L}$ as a function of the intimate contact area $\bar{a}$ for Maugis parameters $\lambda \sim 0$ and ∞, with normalised amplitude and wavelength $\{\alpha,\beta\} = \left\{\sqrt{2}/3, 2\right\}$. The medium dashed, grey-shaded lines indicate the (M-)DMT (E.43a) and JKR (E.42a) response, and the long-dashed lines the (M-)DMT (E.43d) and JKR (E.42b) envelope.

In Fig. 2, the load-area response is presented for wave parameters $\{\alpha,\beta\} = \left\{\sqrt{2}/3, 2\right\}$ (scaled Johnson parameter $\sqrt{\beta/\alpha^2} = 3$) with Maugis parameters $\lambda \sim 0$ and ∞; the closed-form analytical M-DMT (E.43a) and JKR (E.42a) response are indicated by medium-dashed, light- and dark-shaded grey lines, respectively, and their (DMT and JKR) envelopes (E.43d) and (E.42b) by long-dashed lines. The prefix "M-" is dropped for brevity sake. The Johnson parameter is the scaled inverse of the amplitude in the asymptotic expansion of the k'th-order Bessel function (B.10) by a sinusoid (Abramowitz et al., 1988) and the size of the load-area envelope in the DMT- and JKR-limit. In the following, figures of the load-area response use the limit representation in Fig. 2 as a reference. We present the influence of intermediate Maugis parameters $0 < \lambda < \infty$, and the assumption of a continuous intimate contact area on the load-area response next.

4. Methods & approach

In this study, we combine (semi-)analytical and numerical analysis. The semi-analytical results are obtained by means of numerical rootfinding (Inc., 2023) with Eq. (15b) of the adhesive strip m for intimate contact areas $0 < \bar{a} \leq 6$. The infinite sum on the RHS

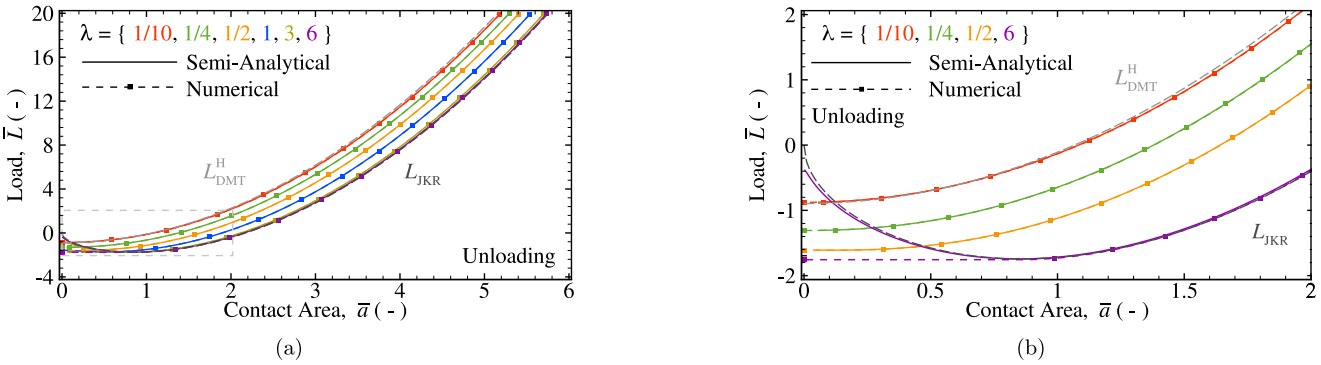

Fig. 3. Normalised load $\bar{L}$ as a function of the intimate contact area $\bar{a}$ for Maugis parameters λ =1/10, 1/4, 1/2, 1, 3 and 6, in smooth cylindrical contact with normalised amplitude and wavelengths $\{\alpha, \beta\} = \{0, -\}$. The medium dashed, grey-shaded lines indicate the (M-)DMT (E.44) and JKR (E.42) response with Maugis parameters λ =1/10 and $\sim \infty$, respectively. The results for intermediate Maugis parameters λ =1 and 3 are omitted from (b) for clarity sake.

of Eq. (15b) is approximated by a finite sum with $k_{max} = 10^3$. The numerical model adopted is the one presented by Van Dokkum and Nicola (2019) and Pérez-Ràfols et al. (2023), that employs the Green's Function Molecular Dynamics (GFMD) technique and discrete Fourier transform (Frigo and Johnson, 2005) to achieve an efficient algorithm. The GFMD technique is a boundary-element method that permits one to reduce the dimensions of the problem such that only the profile of the substrate is modelled. Each dimensionless time-step, the position (Störmer-)Verlet algorithm (Störmer, 1912) is used to compute, through damped dynamics, the new displacement $u(x)$ of n_x equispaced nodes, that discretise the profiles. The (wavy) cylinder is first loaded to the total load $\bar{L}_{max} = 20$, that is subsequently reduced till jump-out of contact at the tensile load $-\bar{L}_p$. The attractive traction is described by the Dugdale-Maugis model (Dugdale, 1960; Maugis, 1992) in our numerical analysis as well. Adhesion is here implemented using a first-order approximation in the gap, in a manner similar to that presented by Medina and Dini (2014). Here, we present the semi-analytical and numerical result for smooth cylindrical contact first. The (semi-)analytical results are validated with, and offset by, numerical results for the mixed-boundary value problem (3). By contrasting the result for smooth cylinders, we present the differences between methods, *i.e.* where instabilities occur, and provide validation to the semi-analytical method here derived. Moreover, we will use these results to compare smooth and wavy contact and isolate the characteristics of waviness.

In Fig. 3, the load-area response is presented for Maugis parameters $\lambda = 1/10$, 1/4, 1/2 1, 3 and 6, in smooth cylinder contact with wave parameters $\{\alpha, \beta\} = \{0, -\}$ during unloading; the JKR and DMT limits (E.42) and (E.44) are indicated with medium dashed, grey-shaded lines, with Maugis parameters $\lambda \sim \infty$ and 1/10, respectively; the semi-analytical and numerical result, that we obtain via the GFMD method, are indicated by solid and dashed, coloured lines, respectively. The solid-coloured, square markers are guides to the eye of the numerical result. The numerical coincides with the semi-analytical result over the whole load-area response except for jump-out of contact, that is appreciable for Maugis parameters $\lambda = 3$ and 6. As expected (Johnson and Greenwood, 2008), the limit responses (E.42) and (E.44) overlap the semi-analytical curves for Maugis parameters $\lambda = 1/10$, and 3 and 6, respectively. The latter is visible in Fig. 3b. We will investigate in the following whether the overlap of analytical and numerical result also hold with roughness, as this is debatable (Zhu et al., 2021).

In order to present contact instability, the load-area response near jump-out of contact is presented again in Fig. 3b, with a shorter range of intimate contact area $0 < \bar{a} \leq 2$; the area of the plot is indicated by a light grey, dashed rectangle in Fig. 3a. Jump-out of contact is recognisable by the dashed, horizontal line of the numerical result that deviates from the same coloured, solid line of the semi-analytical result. Under load control, a mechanical instability occurs because no stable equilibrium is attainable once the load-area gradient $\partial L/\partial a$ becomes negative (*i.e.* at a turning point); no additional external work is necessary to reduce the contact area. The minimum intimate contact area $\bar{a}$ increases with decreasing Maugis parameter $\lambda \ll 3$ because the size of the adhesive strips $|c - a|$ becomes of the same order of magnitude; while the adhesive traction σ decreases for a constant work of adhesion $\Delta\gamma$, the total load L for intimate contact area $\bar{a} \ll 1$ increases. The semi-analytical method enforces intimate contact area $0 \approx \bar{a} < 1$ and hence unstable, static equilibrium.

We perform the numerical simulations with the cylindrical radius $R = \mathcal{L}/10$, where $\mathcal{L}$ is the periodic width. We intend to model the response of an isolated cylinder, by reducing the effects of the inherent periodicity of the discrete Fourier transform (Frigo and Johnson, 2005), whilst retaining computational tractability. We show by means of Fig. 3 that the numerical model (Van Dokkum and Nicola, 2019; Pérez-Ràfols et al., 2023) is suitable for comparison with the semi-analytical result of wavy contact. Moreover, the spatial discretisation $n_x = 2^{15}$ ensures convergence for the loads $-L_p \leq L \leq L_{max}$, and wave parameters $\{\alpha, \beta\} = \{0, 9/8\}, \ldots, \left\{\sqrt{2}/3, 2\right\}$ for different Maugis parameters $\lambda = 1/10, \ldots, 6$, that we present in the following.

5. Wavy contact

We start by analysing the effect of geometry of the waviness that is characterised by the normalised amplitude α and wavelength β, and the Johnson parameter $\sqrt{2\beta/(\pi\alpha)^2}$ that depends on them. In Figs. 4a, b and c, the load-area response is given for the Maugis parameters $\lambda = 1/10$, 1/4, 1/2, 1 and 3, with wave parameters $\{\alpha, \beta\} = \left\{2\sqrt{2}/8, 2\right\}$, $\left\{\sqrt{2}/3, 2\right\}$ and $\left\{2\sqrt{2}/8, 9/8\right\}$; the DMT envelope with the Maugis parameter $\lambda \sim 0$ and JKR envelope with $\sim\infty$ are represented by long dashed, grey-shaded lines and differ slightly between Figs. 4a, and b and c. The scaled Johnson parameter $\sqrt{\beta/\alpha^2} = 4$ and 3 in Fig. 4a, and b and c, respectively, the normalised amplitudes $\alpha = 2\sqrt{2}$ and $2\sqrt{2}/8$ varies, and the normalised wavelength $\beta = 2 \cdots 9/8$ decreases from Fig. 4a to c. We restrict our observations to the load-area response limits of the semi-analytical result first.

As expected, the semi-analytical load-area trajectory for Maugis parameter $\lambda = 3$ is very close to the JKR-limit response $\lambda \sim \infty$ of Eq. (E.42a), that is indicated by a dark-grey shaded, medium-dashed line in Fig. 4. We observe that the difference between the load-area trajectory with the Maugis parameter $\lambda = 3$ and the JKR response with $\lambda \sim \infty$ increases with scaled Johnson parameter $\sqrt{\beta/\alpha^2} = 4 \cdots 3$ and normalised wavelength $\beta = 2 \cdots 9/8$. Hence it is most noticeable in Fig. 4c for the lowest Johnson parameter $\sqrt{2\beta/(\pi\alpha)^2} = 3\sqrt{2}/\pi$.

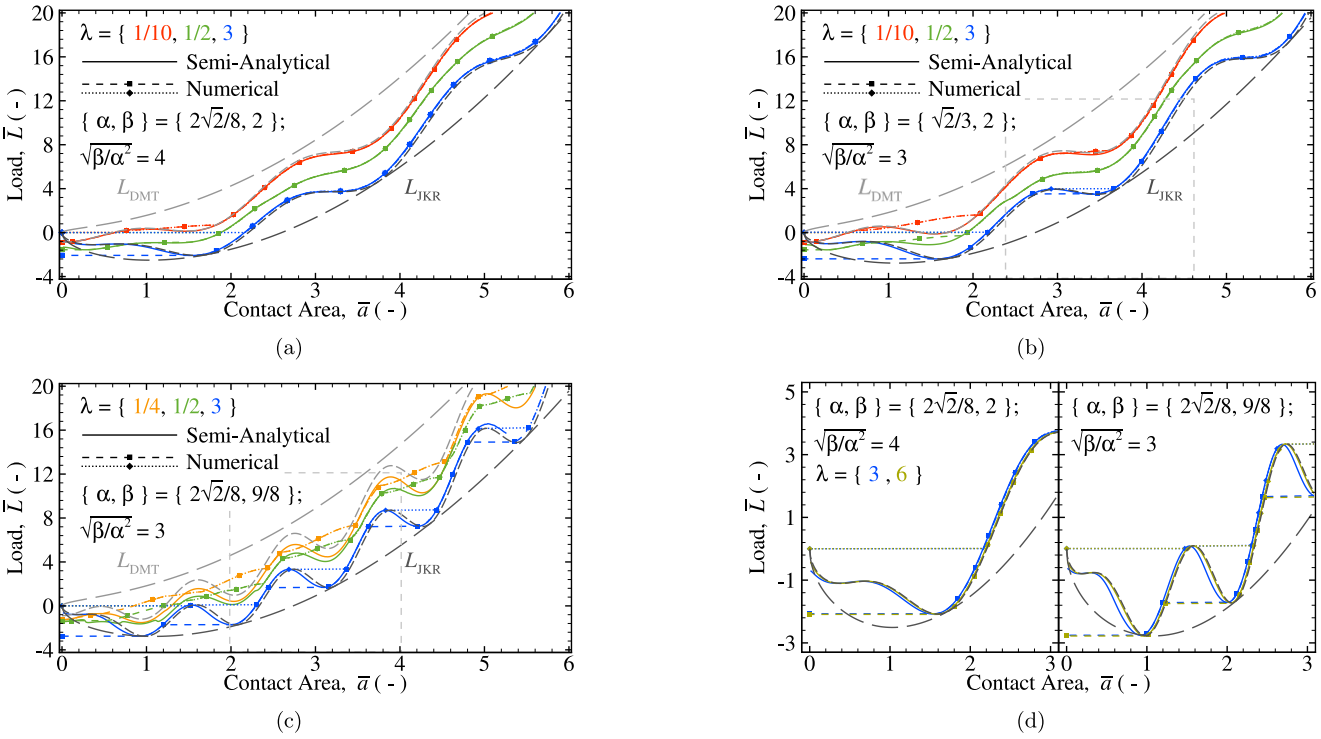

Fig. 4. Normalised load $\bar{L}$ as a function of the contact area $\bar{a}$ for Maugis parameters $\lambda = 1/10$, $1/4$, $1/2$ and 3, with wave parameters (a,d) $\{\alpha,\beta\} = \left\{2\sqrt{2}/8, 2\right\}$, (b) $\left\{\sqrt{2}/3, 2\right\}$ and (c,d) $\left\{2\sqrt{2}/8, 9/8\right\}$. The numerical results during loading are indicated by dotted, coloured lines and diamond-shaped markers, and during unloading by dashed, coloured lines and square markers. The medium and long, grey-shaded lines indicate the limit responses (E.42a) and (E.43a), and the upper and lower envelopes (E.42b) and (E.43d), with Maugis parameters $\lambda = 1/10$, $\sim \infty$, and ~ 0 and $\sim \infty$, respectively. The result for Maugis parameter $\lambda = 6$ is added in (d) for comparison sake.

Only when the Maugis parameter $3 \ll \lambda$, *i.e.* $\lambda = 6$ in Fig. 4d, do the semi-analytical and JKR response coincide. These observations are in line with the reasoning by Zhu et al. (2021), who state that as the interface toughens with roughness the Maugis parameter λ needed to approach the JKR-limit increases. The semi-analytical response for Maugis parameters $\lambda = 1/10$ and $1/4$ approach the DMT-limit response $\lambda \sim 0$ in Eq. (E.43d), as indicated by a light-grey shaded, medium-dashed line in Fig. 4. We note that, in general, the load-area response is bound by the upper and lower envelope, (E.42b) and (E.43d), respectively. We deliberately ignore the scaled intimate contact area $2\pi\bar{a}/\beta$ that approach zero, where the asymptotic expansion of the Bessel function fails (See Appendix E).

In Fig. 4, the numerical result during loading is indicated with dotted lines and diamond-shaped markers; and during unloading, with dashed lines and square markers. The solid-coloured markers are guides to the eye of the numerical result. The fraction of the load-area trajectory where semi-analytical and numerical result coincide increases with Maugis parameter λ, Johnson parameter $\sqrt{2\beta/(\pi\alpha)^2}$ and dimensionless wavelength β (here, we ignore mechanical instabilities). Only for the Maugis parameters $\lambda = 3$ and 6 there are roughness-induced mechanical instabilities as indicated with horizontal, dashed lines in Figs. 4b, c and d, without markers. The instabilities start, as expected, at turning points. Instabilities thus occur at higher(/lower) load $\bar{L}$ during loading (/unloading) when the amplitude α increases and/or the wavelength $\sqrt{\beta}$ decreases (Kesari et al., 2010). At low Maugis parameter, no instabilities are observed.

We observe a disparity between numerical and semi-analytic result. This is most noticeable in Fig. 4c for wave parameters $\{\alpha,\beta\} = \left\{2\sqrt{2}/8, 9/8\right\}$ and Maugis parameters $\lambda = 1/4, \ldots, 1$; instead of a roughness-induced mechanical instability, a monotonic and

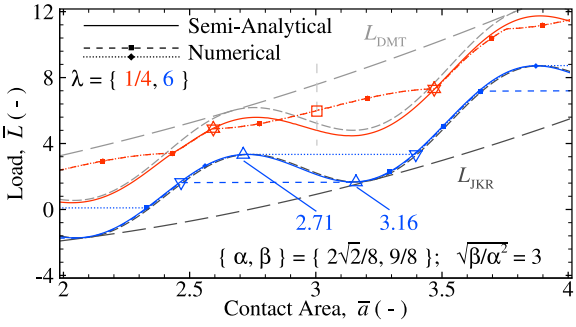

Fig. 5. The normalised load $\bar{L}$ as a function of the intimate contact area $\bar{a}$ with wave parameters $\{\alpha,\beta\} = \left\{2\sqrt{2}/8, 9/8\right\}$ for Maugis parameters $\lambda = 1/4$ and 6. The medium and long, grey-shaded lines indicate the limit responses (E.42a) and (E.43a), and the upper and lower envelopes (E.42b) and (E.43d), with Maugis parameters $\lambda = 1/4$ and $\sim \infty$, respectively. The minimum and maximum continuous, intimate contact area, that border the mechanical instability and cavitation, are indicated by Delta- and gradient-symbols during loading, and *vice versa* during unloading.

continuous change of the total, numerical intimate contact area is observed. These are marked by dashed-dotted lines with square and diamond-shaped markers. Even so, we find that our numerical result corroborates our semi-analytical solution in Section 3 for a broad range of roughnesses $\{\alpha,\beta\}$ and loads $\bar{L}$. To better visualise contact behaviour, we present in Fig. 5 two of the cases with wave parameters $\{\alpha,\beta\} = \left\{2\sqrt{2}/8, 9/8\right\}$ in Fig. 4c but for a shorter range of intimate contact area $2 \leq \bar{a} \leq 4$; the Maugis parameters are $\lambda = 1/4$ and 6; the limit responses (E.42a) and the upper bound of the envelope (E.43d) correspond with the Maugis parameter $\lambda = 1/4$; and, are indicated

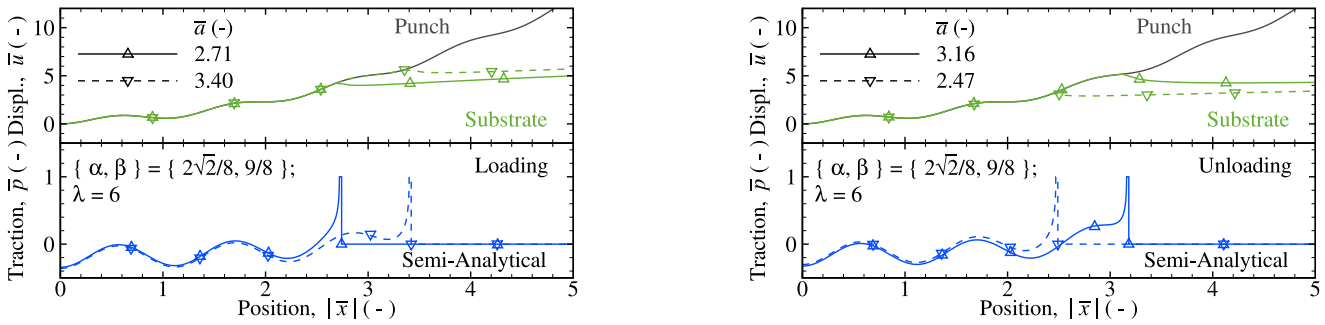

Fig. 6. The semi-analytical, normalised displacement $\bar{u}$ and normalised traction $\bar{p}$ as a function of the normalised position $|\bar{x}|$ with roughness parameters $\{\alpha,\beta\} = \left\{2\sqrt{2}/8, 9/8\right\}$ and Maugis parameter $\lambda = 6$, during (a) loading and (b) unloading. The intimate contact area (a) $\bar{a} \approx 2.71$ and 3.40, and (b) 3.16 and 2.47 as indicated by blue coloured, open Delta- and gradient-shaped marker, respectively, on the load-area trajectory in Fig. 5. The grey solid line indicates the profile of the rigid punch and the green lines the profiles of the substrate.

by medium and long dashed, light-grey lines, respectively. The numerical result for Maugis parameter $\lambda = 6$ shows a discontinuous, and for $\lambda = 1/4$ a continuous, change in total intimate contact area. The numerical load-area trajectory of the latter Maugis parameter is monotonous and a single-valued function. These two cases exemplify two distinct behaviours, which are discussed in detail in the following two sections.

5.1. Mechanical instabilities

The blue curves with triangle-shaped markers in Fig. 5, which correspond to a high Maugis parameter, exhibit mechanical instabilities at intimate contact area $\bar{a} = 2.71$ and 3.16 during loading and during unloading, respectively. The semi-analytical load-area response with a negative slope is unstable and hence inaccessible to the quasi-static, numerical solution (See Section 4). The minimal(/maximal), continuous intimates contact area past the given instability is indicated with a gradient-shaped marker in Fig. 5. The wave profile leads to loading-unloading hysteresis and energetically irrecoverable deformation. Adhesive dissipation in wavy contact is the total energy loss by instabilities on the Hertzian (See Section 4) and wave length scale. With Equation (3b) and the normalisation (13a), combining Eqs. (7) and (A.4b), we give the normalised total traction as

$$\bar{p}(\bar{x}) = \frac{2}{\pi}\tan^{-1}\left(\bar{a}\sqrt{\frac{m^2-1}{\bar{a}^2-\bar{x}^2}}\right)\cdots \qquad (16)$$
$$\cdots - \frac{\sqrt{\bar{a}^2-\bar{x}^2}}{2\lambda}\left(1+\frac{2\pi\alpha}{\beta\bar{a}}\int_0^{\frac{2\pi\bar{a}}{\beta}} J_0(t)\cos\left(\frac{\bar{x}t}{\bar{a}}-\frac{2\pi\bar{x}}{\beta}\right)\mathrm{d}t\right),$$

inside the intimate contact area at $|\bar{x}| \le \bar{a}$; unity inside of the adhesive strip at $\bar{a} < |\bar{x}| \le m$; and, zero outside of contact at $m < |\bar{x}|$. We present the semi-analytical substrate $u(x)$ and traction $p(x)$ profile just before and just after the given instability during loading in Fig. 6a and unloading in b. The solid and dashed line correspond with the intimate contact areas $\bar{a}$ just before and after the given instability, that are 2.71 and 3.40 during loading, and 3.16 and 2.47 during unloading; and, the Delta- and gradient-shaped makers are guides to the eye. The rigid punch profile is indicated by a grey, solid line and the semi-analytical result with solid and dashed lines. Note that the difference in intimate contact before and after the given instability is the same during loading and unloading for Maugis parameter $3 \ll \lambda$ in Fig. 4d, and is $\Delta\bar{a} \approx 0.69$ in this specific case.

The loci of the mechanical instabilities during unloading in the JKR-limit are discussed qualitatively by Guduru (2007): when the edges of contact at $x = |a|$ approach wave crests, an additional decrease in load, $\mathrm{d}L < 0$, is necessary compared with smooth contact to reduce the contact area, $\mathrm{d}a < 0$, because the pressure just inside of contact, *i.e.* the adhesive load L_a, increases with the total traction, $0 < \mathrm{d}p(|x| \lessapprox a)$. Here, the definition of crests and valleys follows the classical, contact mechanical Cartesian coordinate system used by Guduru and Bull (2007), Guduru (2007) and Waters et al. (2009), where the positive normal displacement compresses the substrate. Furthermore, solely in the JKR-limit the intimate contact and total contact area are synonyms. Once the edges of contact at $x = |a|$ traverse the crests, the total traction just inside contact decreases, $\mathrm{d}p(|x| \lessapprox a) < 0$, and the total load increases, $0 < \mathrm{d}L$. Meanwhile the total traction far inside the contact area $p(|x| \ll a)$ is approximately constant. Under load control, the stored, potential (*i.e.* elastic) energy per unit contact area is then greater than the work of adhesion $\Delta\gamma$; no additional external work is necessary to reduce the contact area. Hence a mechanical instability occurs. We find the same mechanism acts during loading (See Fig. 6a) where now the edges of contact at $x = |a|$ traverse a valley, the total traction just inside contact decreases, $\mathrm{d}p(|x| \lessapprox a) < 0$, and the total load increases, $0 < \mathrm{d}L$. The traction just inside of contact $p(|x| \lessapprox a)$, just prior the instability, thus reaches a minimum during indentation and a maximum during retraction in Figs. 6a and b, respectively.

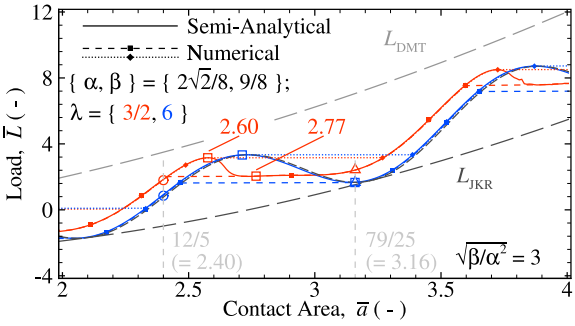

Fig. 7. Normalised load $\bar{L}$ as a function of the intimate contact area $\bar{a}$ with wave parameters $\{\alpha,\beta\} = \left\{2\sqrt{2}/8, 9/8\right\}$ for Maugis parameters $\lambda = 3/2$ and 6. The medium dashed, dark grey line indicates the JKR-limit (E.42a) and the long, dashed lines the upper and lower envelopes (E.42b) and (E.43d), with Maugis parameters $\lambda = 3/2$ and $\sim\infty$, respectively. The minimal and maximum continuous, intimate contact area, that border the mechanical instabilities, are indicated by open, square markers during loading and unloading, respectively.

In Fig. 7, the load-area response is given for a case with Maugis parameter $\lambda = 3/2$ and wave parameters $\{\alpha,\beta\} = \left\{2\sqrt{2}/8, 9/8\right\}$; the case with Maugis parameters $\lambda = 6$ coincides with the JKR solution, while that with $\lambda = 3/2$ departs from it. Furthermore, for Maugis parameter $\lambda = 3/2$, the intimate contact area jumps Δa caused by an instability during loading and unloading differ. These jumps start at

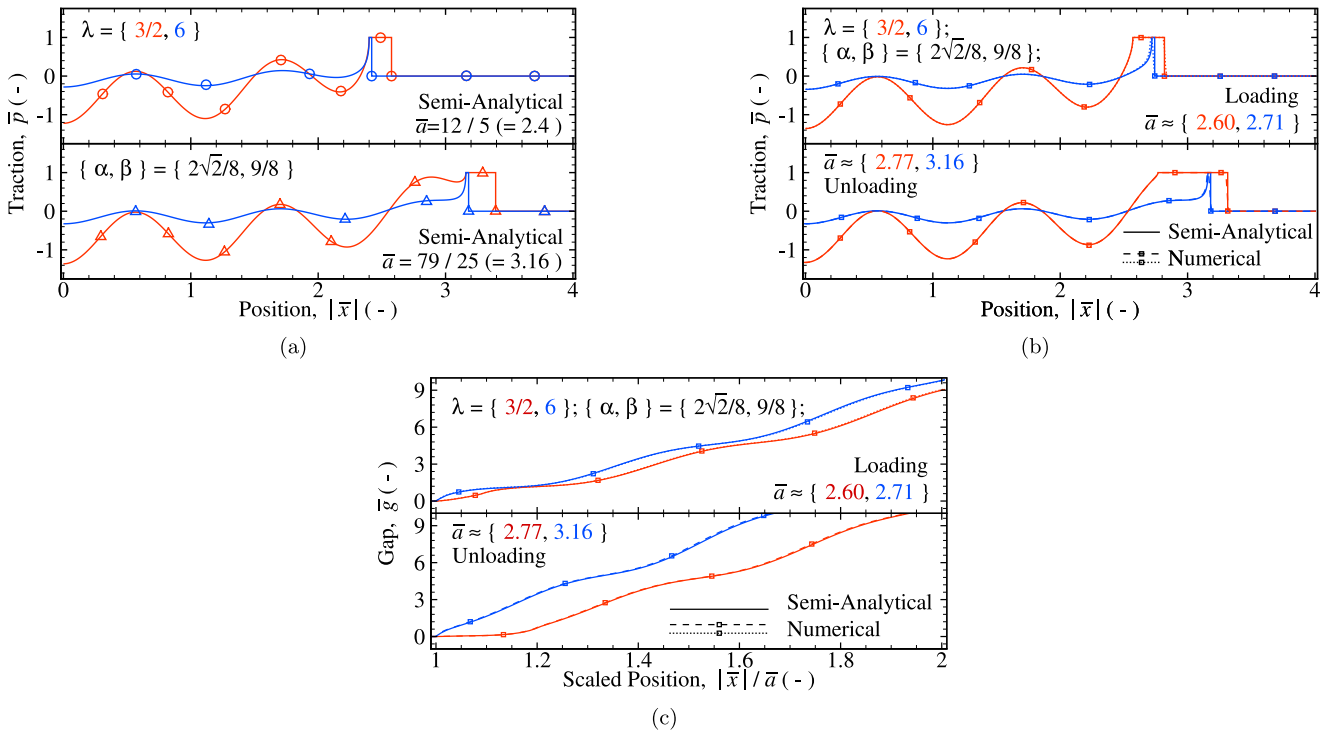

Fig. 8. (a) Normalised traction $\bar{p}$ as a function of the normalised position $\bar{x}$ with intimate contact areas $\bar{a} = 12/5$ and $79/25$ as marked by dashed grey, vertical lines, and open circular and triangle-shaped markers, respectively, for the same Maugis parameters $\lambda = 3/2$ and 6 in Fig. 7. (b) Normalised traction $\bar{p}$ as a function of the normalised position $|\bar{x}|$, and (c) normalised gap $\bar{g}$ as a function of the scaled, normalised position $|\bar{x}|/\bar{a}$ for the intimate contact areas $\bar{a} \approx 2.60$, 2.71, 2.77 and 3.16 as indicated by open square-shaped markers in Fig. 7.

intimate contact areas $\bar{a} = 2.60$ and 2.77 during loading and during unloading, respectively, as indicated by red, open-square markers in Fig. 7.

From Fig. 7 it is apparent that the intimate contact area traversed in a mechanical instability, Δa, is larger during loading than during unloading for Maugis parameter $\lambda = 3/2$; the jump in contact area Δa during loading(/unloading) decreases(/increases) with Maugis parameter λ. Hence the area traversed during a given instability for Maugis parameter $\lambda < 3$ depends on the loading direction. We address the decrease in intimate contact area from $\bar{a} = 3.16$ to 2.77 with decreasing Maugis parameter $\lambda = 6$ and $3/2$ during unloading first. Subsequently, we discuss the asymmetry in intimate contact area jump Δa between loading and unloading, that increases with decreasing Maugis parameter λ ($3/2$ herein).

We present the semi-analytical traction profiles $p(x)$ before and after the given instabilities for Maugis parameters $\lambda = 3/2$ and 6 in Fig. 8a. These loci on the load-area trajectories with intimate contact areas $\bar{a} = 12/5\,(= 2.4)$ and $79/25\,(= 3.16)$ are indicated in Fig. 7 by circular and Delta-shaped markers, respectively, and vertical light-grey, dashed lines. In Figs. 8b and c, we give the traction $p(x)$ and gap $g(x)$ profile, respectively, for Maugis parameters $\lambda = 3/2$ and 6 just before the turning point of the given instability during loading (top) and unloading (bottom). These loci with the intimate contact areas $\bar{a} \approx 2.60$ and 2.77, and $\bar{a} \approx 2.71$ and 3.16 for Maugis parameters $\lambda = 3/2$ and 6, respectively, are indicated with open, square markers on the load-area trajectories in Fig. 7 as well. The semi-analytical solution and the numerical result in Figs. 8b and c are indicated by solid, and medium-dashed and dotted, coloured lines, respectively. The open markers in Fig. 8a correspond with the different loci on the load-area response in Fig. 7, and are guides to the eye of the numerical result in Figs. 8b and c. Note that only the traction profiles with intimate contact areas $\bar{a} = 3.16$ and 2.77 for the Maugis parameter $\lambda = 3/2$ change between the bottom halves of Fig. 8a and b, and predominantly near the edges of intimate contact.

Comparing the traction profile $p(x)$ for the Maugis parameter $\lambda = 3/2$ with intimate contact areas $\bar{a} \approx 2.77$, in Fig. 8b, with that for Maugis parameter $\lambda = 6$ and intimate contact area $\bar{a} = 3.16$ in Figs. 8a and b, we find that the adhesive strips $|c - a|$ increase with a decreasing Maugis parameter λ during unloading. Only the intimate contact a decreases and the contact area c remains approximately constant for the Maugis parameter $\lambda = 3/2$, which one observes comparing Figs. 8a and b for the intimate contact areas $\bar{a} = 3.16$ and 2.77. Secondly, the local profile gradient $\partial f/\partial x$ decreases between the local valleys and crests (See Fig. 1). Whereby in combination with a higher total load L, the gap gradient $\partial g(a < |x| \leq c)/\partial x$ decreases with Maugis parameter $\lambda = 6 \cdots 3/2$ in Fig. 8c. The scaling of the normalised position $\bar{x}$ with the normalised contact area $\bar{a}$ does not change succession in gap gradient $\partial g/\partial x$ with Maugis parameter λ. Hence, while the adhesive traction σ decreases with Maugis parameter λ, the width of the adhesive strip $|c - a|$ increases with a decreasing gap outside of the intimate contact, $g(a < |x| \leq c)$. Thirdly, we observe that the traction at the edges of contact, inside of the intimate contact area, $0 < p(|x| \lessapprox a) \approx \sigma$ as the maximum traction inside of contact $\propto \alpha/(\lambda\beta)$ (See Eq. (16)); and, increases with decreasing Maugis parameter $\lambda = 6 \ldots 3/2$. An additional decrease in the total load, $\mathrm{d}L < 0$, thus is necessary to reduce the intimate contact area, $\mathrm{d}a < 0$. Wherefore the intimate contact areas $\bar{a} \approx 3.16 \cdots 2.77$, just before a mechanical instability during unloading, decrease with Maugis parameter $\lambda = 6 \cdots 3/2$ in Fig. 7. Moreover, the intimate contact areas $a \approx 2.42$ and 2.45 differ less during unloading after the given instability (between Maugis parameters $\lambda = 3/2$ and 6, respectively) than before. Hence the jump in intimate contact area Δa decreases with Maugis parameter λ during unloading.

The asymmetry between loading and unloading for Maugis parameter $\lambda = 3/2$ occurs because the surface gradient $\partial f/\partial x$ in adhesive contact is larger during loading, when the contact edges pass crests, and smaller during unloading when the contact edges pass valleys (See Fig. 1). This is in line with the differences in profiles between

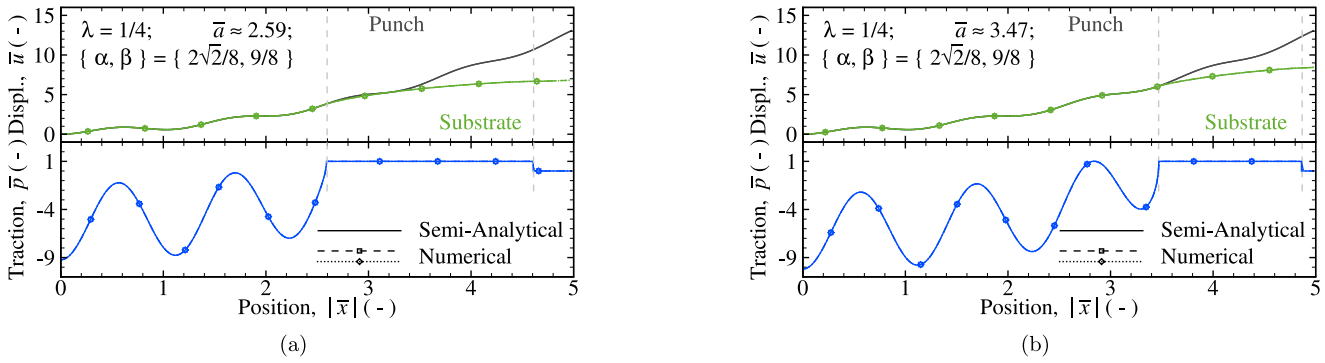

Fig. 9. The normalised displacement $\bar{u}$ and normalised traction $\bar{p}$ as a function of the normalised position $|\bar{x}|$ with roughness parameter $\{\alpha,\beta\} = \left\{2\sqrt{2}/8, 9/8\right\}$ and Maugis parameter $\lambda = 1/4$ during (a) loading and (b) unloading. The intimate contact area (a) $\bar{a} \approx 2.59$ and (b) 3.47 as indicated by red coloured, star-shaped markers on the load-area response in Fig. 5. The light grey, dashed lines indicate the adhesive strip $a < |x| \leq c$.

loading and unloading, which we show in Fig. 8c. Secondly, the adhesive strip before the instability is smaller during loading than during unloading (See Fig. 8b), which has an appreciable effect as the adhesive strips becomes generally wider with decreasing Maugis parameter λ. We find that the asymmetry in intimate contact area jump Δa is because of the finite range of adhesion δ. In JKR-theory adhesive and intimate contact coincide, $a \approx c$ for Maugis parameter $\lambda = 6$. Instabilities thus are insensitive to the gap gradient $\partial g/\partial x$ outside of intimate contact, *i.e.* of pure geometrical origin. In contrast, for finite-range adhesion (here $\lambda = 3/2$), the difference in local surface $\partial f/\partial x$ between loading and unloading makes the area traversed Δa in a given instability loading-direction dependent.

5.2. Cavitation

With Maugis parameter $\lambda = 1/4$, as indicated by the red curves with star-shaped markers in Fig. 5, the contact cavitates between intimate contact areas $\bar{a} \approx 2.59$ and 3.47. Here, *cavitation* is defined as the occurrence of gaps under tensile traction over strips that are surrounded by intimate contact on either side. Cavitation is indicated by red, dashed-dotted lines with solid, red-coloured markers in Fig. 5. For the wave roughness herein, both the semi-analytical and numerical, intimate and adhesive contact areas vary continuously with cavitation. Cavitation leads to a monotonic, numerical load-area response, *i.e.* without any turning point. The minimum(/maximum) and maximum(/minimum) continuous, intimate contact areas in Fig. 5, prior and past the given cavitation, are indicated by Delta- and gradient-shaped markers, respectively, during (un)loading. The numerical load-area trajectories coincide and the deformation is energetically recoverable. Note that cavitation prevents a potential mechanical instability because the semi-analytical result for Maugis parameter $\lambda = 1/4$, which cannot capture cavitation, exhibits a region with negative load-area gradient $\mathrm{d}L/\mathrm{d}a < 0$. There instability would occur under load control when continuous intimate contact is enforced.

We present in Fig. 9 the substrate $u(x)$ and traction profile $p(x)$ with roughness parameters $\{\alpha,\beta\} = \left\{2\sqrt{2}/8, 9/8\right\}$ and Maugis parameter $\lambda = 1/4$ just before and after cavitation in Fig. 5, *i.e.* with the continuous intimate contact area $\bar{a} = 2.59$ in Fig. 9a and 3.47 in b; the numerical result during loading is indicated with dotted lines and diamond-shaped markers; and during unloading, with dashed lines and square markers. These markers are guides to the eye of the numerical result. The semi-analytical result is indicated with solid lines and void of markers. The vertical, light-grey dashed lines indicate the sizes of the adhesive strips $|c - a|$. The semi-analytical and numerical result, and the loading and unloading trajectory coincide in Fig. 9

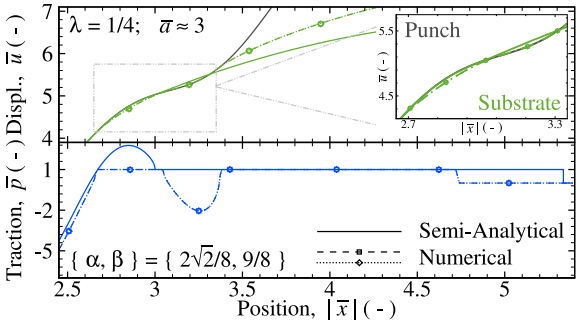

Fig. 10. The normalised displacement $\bar{u}$ and normalised traction $\bar{p}$ as a function of the normalised position $|\bar{x}|$ with roughness parameters $\{\alpha,\beta\} = \left\{2\sqrt{2}/8, 9/8\right\}$ and Maugis parameter $\lambda = 1/4$ during loading and unloading. The intimate contact area $\bar{a} \approx 3$ as indicated by a red, open-square marker on the numerical load-area response in Fig. 5.

as expected. Notable though is that the size of contact c is approximately constant during cavitation, whereby the total intimate contact area a increases(/decreases) and thus the adhesive strips $|c - a|$ decrease(/increase) during (un)loading.

Upon loading, the contact cavitates when the adhesive strips $a < |x| \leq c$ encompass the two adjacent crests and valleys at each site with $g(a < |x| \leq c) < \delta$ for intimate contact area $\bar{a} \approx 2.59$. The gap on the crests nearest the edges of intimate contact, yet outside of intimate contact, vanishes $g(3 < |\bar{x}| < 3.5) \sim 0$ in Fig. 9a. When the load increases further, $0 < \mathrm{d}L$, these crests come into intimate contact, while the adjacent valleys remain separated. Hence the inner valleys form cavities. Continuous contact is attained again, once these gaps at valleys are closed in Fig. 9b. During unloading in Fig. 5, the maximum traction inside of intimate contact, which occurs in the valleys, with $2.5 < |\bar{x}| < 3$ in Fig. 9b, nearest the edges of intimate contact, keeps increasing. Eventually, it matches the adhesive traction $p(|x| < a) \sim \sigma$ for intimate contact area $\bar{a} \approx 3.47$. When the load decreases further, $\mathrm{d}L < 0$, the valleys just inside of intimate contact cavitate, while the surrounding crests remain in intimate contact. Continuous contact is attained again once the outer crests go out of intimate contact in Fig. 9a. During cavitation the position of the outer most edge of the adhesive strips $|x| = c$ thus moves little while the total, intimate contact area a changes significantly.

The disparity in load-area trajectory of Figs. 4 and 5 between semi-analytical and numerical result during cavitation is of interest. We thus present in Fig. 10, the substrate $u(x)$ and traction profile $p(x)$ for one such case, *i.e.* with roughness parameters $\{\alpha,\beta\} = \left\{2\sqrt{2}/8, 9/8\right\}$ and Maugis parameter $\lambda = 1/4$ for the total, intimate contact area $\bar{a} \approx 3$; the profiles $u(x)$ and $p(x)$ correspond with the intersects of the semi-analytical and numerical result, and the dashed light-grey vertical line of $\bar{a} = 3$, where the numerical result in Fig. 5 is marked with a red, open-square marker. The semi-analytical gap $g\left(a \lessapprox |x| < c\right) < 0$ in Fig. 10 is negative on the crests nearest to the edges of intimate contact because the Maugis analysis does not prevent interpenetration inside of the adhesive strip. Furthermore, the maximum traction of the semi-analytical result exceeds the adhesive traction $\sigma < p\left(|x| \lessapprox a\right)$. The traction boundary condition is not enforced for all contact areas c as a continuous, intimate contact area a is the only requirement. The Maugis analysis does not limit the adhesive traction inside of intimate contact $p(|x| < a)$ either (See Section 2). With continuous intimate contact, the displacement $u\left(|x| \lessapprox a\right)$ in valleys just inside of intimate contact increases, and hence traction $p(a < |x| \leq c)$ exceeds the maximum traction σ. Wherefore the gradient of the semi-analytical load-area trajectory $\partial L/\partial a$, *e.g.* in Fig. 5 for Maugis parameter $\lambda = 1/4$, switches sign with of the excess tensile traction $\sigma < p\left(|x| \lessapprox a\right)$ on the valleys in intimate contact and the large semi-analytical contact area c. The semi-analytical result thus is incorrect during cavitation.

For the numerical results, the morphology of the contact area is an outcome of the mixed boundary-value problem (3). The inequality (3a) is ensured, the crests at $3 < |\bar{x}| < 3.5$ in Fig. 10 come in repulsive, intimate contact, and the valleys at $2.5 < |\bar{x}| < 3$ remain in tensile, adhesive contact. At locations where the semi-analytical traction $\sigma < p\left(a \lessapprox |x|\right)$, intimate contact is destroyed and local separation (*i.e.* cavitation) occurs with a numerical gap $0 < g < \delta$ (See the insert in Fig. 10). This numerical result thus appears to be the only correct solution during cavitation.

Upon loading, the contact cavitates when crests inside the adhesive strips come into intimate contact. The adhesive strip must thus span at least a valley and a crest outside of intimate contact; and, upon unloading, valleys inside of intimate contact go out of intimate contact. Inside of intimate contact, a valley thus is under maximum tension and an adjacent crest remains in more compressive intimate contact. Hence during loading cavitation occurs because the crests adjacent to intimate contact prevent interpenetration outside of continuous contact; and during unloading, because the tensile traction is limited by the adhesive strength in the valleys. Both occur prior the semi-analytical load-area gradient $\partial L/\partial a$ becomes negative in Fig. 5 and thus prevents instabilities.

5.3. Continuous stable contact

Instabilities are typically associated with high Maugis parameter and cavitation with low Maugis parameter, and intermediate Maugis parameter displays both, either and neither. The transition from continuous contact with instabilities to continuous contact without is trivially observed in *e.g.* Fig. 4b; turning points on the load-area trajectory vanish with decreasing Maugis parameter λ away from JKR-type contact. The load-area trajectory fails to describe the transition from continuous contact with(out) instabilities to cavitation. We present in Fig. 4b two of the cases of wave parameters $\{\alpha,\beta\} = \left\{\sqrt{2}/3, 2\right\}$ in Fig. 4(b) but for a shorter range of intimate contact area $2.5 \leq \bar{a} \leq 4.5$.

For Maugis parameter $\lambda = 1/10$, the contact cavitates between the intimate contact areas $\bar{a} \approx 2.96$ and 3.63 as indicated by a red, square and circular markers, respectively; for $\lambda = 1/2$, the intimate contact area is continuous between the same contact areas $\bar{a} = 29/10 \cdots 39/10$ as indicated by vertical, light-gray dashed lines. According to the semi-analytical results, the slope $\partial L/\partial a$ is always positive for Maugis parameter $\lambda = 1/2$ but sometimes negative for 1/10. In the former case, indeed, no instability occurs; in the latter, the contact cavitates instead,

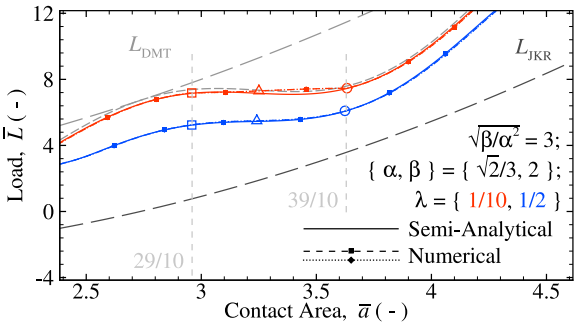

Fig. 11. Normalised load $\bar{L}$ as a function of the intimate contact area $\bar{a}$ with wave parameters $\{\alpha,\beta\} = \left\{\sqrt{2}/3, 2\right\}$ for Maugis parameters $\lambda = 1/10$ and $1/2$. The medium dashed, light grey line indicates the M-DMT limit (E.43a) with Maugis parameter $\lambda = 1/10$, and the long, dashed lines the upper and lower envelopes (E.42b) and (E.43d), with Maugis parameters $\lambda = 1/10$ and $\sim \infty$, respectively.

which leads to an always positive, static load-area gradient, $0 \leq \partial L/\partial a$, of the numerical result. The latter cavitation prevents instabilities. Hence both cases with Maugis parameters $\lambda = 1/10$ and $1/2$ are energetically recoverable.

In Fig. 12, the displacement $u(x)$ and traction profile $p(x)$ are given for the Maugis parameter $\lambda = 1/10$ and $1/2$ with roughness parameters $\{\alpha,\beta\} = \left\{\sqrt{2}/3, 2\right\}$; the load-area loci with the intimate contact areas $\bar{a} \approx 2.96$, 3.25 and 3.63 are indicated with square, Delta-shaped and circular markers, respectively, in Fig. 11. The displacement $u(x)$ is shifted such that the displacement is zero at the edges of intimate contact, *i.e.* $C \equiv \bar{u}(|x| = a)$. The vertical light-grey, dotted and dashed lines indicate the sizes of the contact $m\bar{a} \approx 6.30$ and 4.35 for Maugis parameters $\lambda = 1/10$ and $1/2$, respectively; and, the horizontal lines the normalised interaction ranges $\bar{\delta} = 10$ and 2 at the edges of contact $|x| = c$, respectively.

At the intimate contact area $\bar{a} \approx 2.96$ in Fig. 12a, the adhesive strip $a < |x| \leq c$ for Maugis parameter $\lambda = 1/10$ encompasses four valleys and two enclosed crests; and, for $\lambda = 1/2$, two valleys and crests. With increased intimate contact area $\bar{a} = 2.96 \cdots 3.25$ in Fig. 11 between Figs. 12a and b, the contact remains continuous for Maugis parameter $\lambda = 1/2$ and cavitates for $\lambda = 1/10$; the valleys nearest intimate contact close from the side of intimate contact for Maugis parameter $\lambda = 1/2$, while crests prior in adhesive contact come into compressive contact for $\lambda = 1/10$. Meanwhile the traction $p\left(|x| \lessapprox a\right)$ increases with intimate contact area, $0 < \mathrm{d}a$. Subsequently, with intimate contact areas $\bar{a} = 3.25 \cdots 3.63$ in Fig. 11, as Figs. 12b and c show, the valleys initially out of intimate contact with $\bar{a} \approx 2.96$ closes up for both Maugis parameters $\lambda = 1/10$ and $1/2$. Meanwhile the traction $p\left(|x| \lessapprox a\right)$ becomes tensile with intimate contact area, $0 < \mathrm{d}a$, between intimate contact areas $\bar{a} \approx 2.96$ and 3.63 in Figs. 12b and c. Note again that the size of contact c is approximately constant, $0 \lessapprox \mathrm{d}c$, for both Maugis parameters $\lambda = 1/10$ and $1/2$. Hence contact does not necessarily have to display instabilities at moderate Maugis parameters $1/2 \leq \lambda \leq 3$ to cavitate with lower λ, while the adhesive strips $a < |x| \leq c$ encompasses a valley and a crest. The difference between continuous contact without instabilities and cavitation is whether the maximum tensile traction exceeds the adhesive traction.

Both instability and cavitation are deviations from the semi-analytical result, cavitation occurs for large roughness and smaller Maugis parameter, and is up to here captured only by the numerical analysis. Their difference is remarkable, as instability gives rise to hysteresis and roughness-induced dissipation, while cavitation does neither. It is noteworthy that in Fig. 5 cavitation appears to occur when contacts are stiffer and instability when they are softer. This might seem capricious, but we find that cavitation occurs when contact stiffens because the

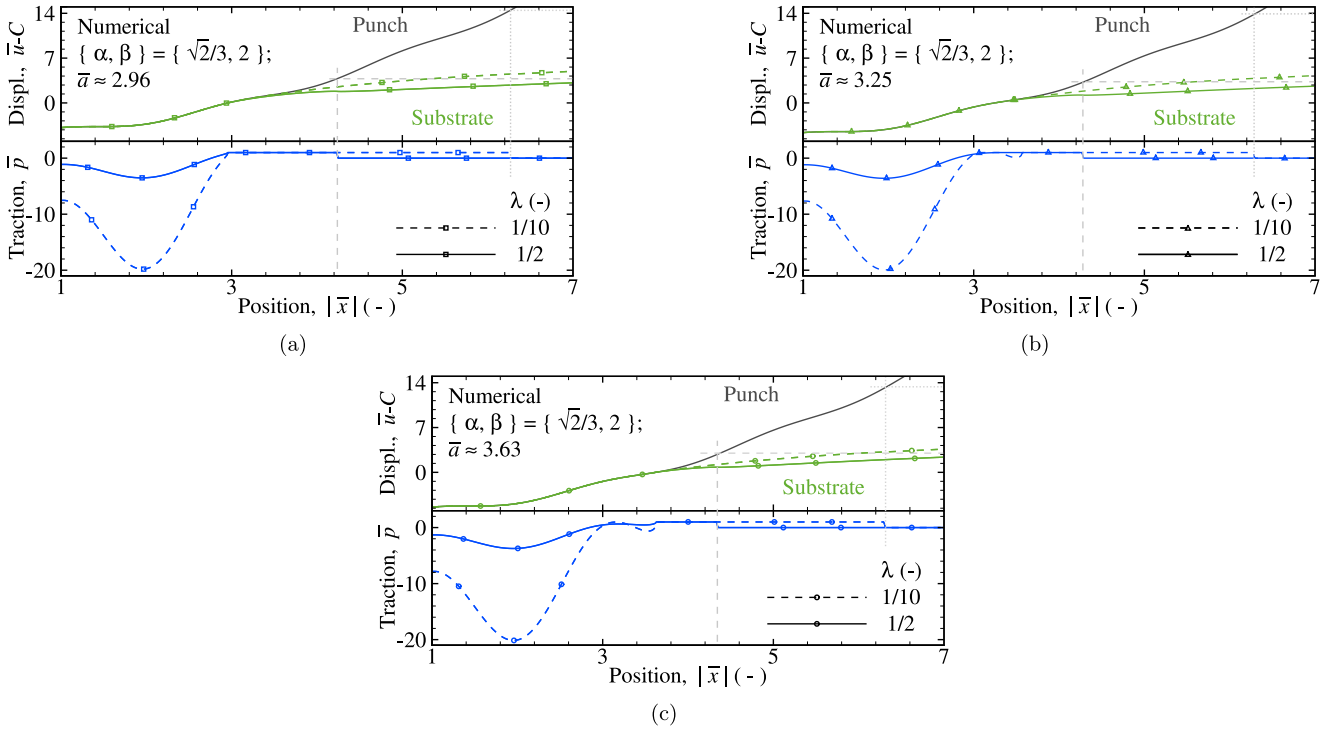

Fig. 12. Shifted, normalised displacement $\bar{u}-C$ and normalised traction $\bar{p}$ as a function of the normalised position $|\bar{x}|$ with roughness parameters $\{\alpha,\beta\}=\left\{\sqrt{2}/3,2\right\}$ and Maugis parameters $\lambda=1/10$ and $1/2$ by dashed and solid lines, respectively. The intimate contact area (a) $\bar{a}\approx 2.96$, (b) 3.25 (c) 3.63 as indicated by square-, Delta-shaped and circular markers in Fig. 11, respectively. The gray dashed and dotted, and dashed-dotted lines indicate the size of the contact c and gap size δ, respectively.

adhesive traction to retain intimate contact increases with decreasing Maugis parameter. *Vice versa*, more compliant contact remains in intimate contact for higher wave roughness and thus instabilities occur. Note that the maximum traction inside of intimate contact scales with wave roughness α/β in Eq. (16). This is in line with the findings by Zhu et al. (2021) for axi-symmetric contact, however the role of interpenetration at crests $g(a<|x|\leq c)<0$ and the negative, semi-analytical load-area gradient $\partial L/\partial a$ were not reported. The validity of any analysis based on continuous contact areas thus depends on the Maugis parameter λ and the wave parameters $\{\alpha,\beta\}$, as together they control the connectivity of the intimate contact area.

5.4. Effect of wave profile on the load-area response

In agreement with previous works (Kesari et al., 2010; Ciavarella, 2016), the Maugis analysis of cylindrical contact with wave profiles approaches the JKR-limit as presented by Guduru (2007) with Maugis parameter $3\ll\lambda$ (See *e.g.* Figs. 4d and 7). We show that the Maugis analysis approaches the M-DMT limit with Maugis parameter $\lambda\ll 1$ (See *e.g.* in Fig. 11 for Maugis parameter $\lambda=1/2$) but not when cavitation occurs. In the former cases, the load-area response is confined within an envelope $\sqrt{\alpha^2/\beta}\sqrt{\bar{a}}$ that is controlled by the Johnson parameter $\sqrt{2\beta/(\pi\alpha)^2}$ (See Fig. 2 and Appendix E). These observations are all limited to a single set of wave parameters $\{\alpha,\beta\}$ and limiting Maugis parameters $\lambda\sim 0$ and $\sim\infty$ and exclude cavitation. It is however of interest whether the local envelope, that depends on at least the Johnson parameters $\sqrt{2\beta/(\pi\alpha)^2}$, encloses also the load-area response for Maugis parameters $1/2\leq\lambda\leq 3$.

We reason that when a sufficient number of wave asperities is in contact the mean load-area response is controlled by smooth cylindrical contact. This already holds in the DMT- and JKR-limits. We thus give the local envelope as

$$\bar{L}\sim\bar{L}^{\mathrm{H}}_{\mathrm{M}}\pm\pi\sqrt{\frac{\alpha^2}{\beta}}\sqrt{\bar{a}}, \tag{17a}$$

with the Hertzian load,

$$\bar{L}^{\mathrm{H}}_{\mathrm{M}}\equiv\bar{L}_{\mathrm{M}}(\bar{a},\{\alpha=0,\beta=-\}), \tag{17b}$$

where the changes in load L_{w} (B.13) and gap $g_{\mathrm{w}}(a<|x|\leq c)$ due to the wave roughness are neglected, with the functional dependence $(\{\bullet\})$ on variables $\bullet$.

In Fig. 13, the load-area response is presented for Maugis parameters $\lambda=1/2$, 1 and $3/2$, with wave parameters $\{\alpha,\beta\}=\left\{\sqrt{2}/3,2\right\}$ and $\left\{2\sqrt{2}/8,9/8\right\}$; the local envelope (17) is indicated by dark-grey, medium dashed lines and marked with symbols $\sim L(\{\lambda\})$. The Maugis parameters $\lambda=1/2\cdots 3/2$ increase from Figs. 13a to c, and the scaled Johnson parameter $\sqrt{\beta/\alpha^2}=3$. The numerical load-area response in Fig. 13 is encompassed by the local envelope $\sim L(\{\lambda\})$ for all wave parameters. For Maugis parameter $1\ll\lambda$, the contact area remains continuous and the load-area responses overlap the local envelope $\sim L(\{\lambda\})$ near their turning points. For wave parameters $\{\alpha,\beta\}=\left\{2\sqrt{2}/8,9/8\right\}$ and $\left\{\sqrt{2}/3,2\right\}$, and Maugis parameters $1/2\leq\lambda\leq 1$, the approximation (17) overestimates the true size of the local envelope. These overestimates, where the load-area response does not intercept the local envelope $\sim L(\{\lambda\})$ (17), coincide with the roughness for which we will show cavitation in Fig. 14. Roughness-induced adhesion is still better approximated when one uses the correction provided by Eq. (17a) than the smooth contact solution for Maugis parameters $\lambda\leq 1$. The Johnson parameter $\sqrt{2\beta/(\pi\alpha)^2}$ might thus be a good approximation for the contribution of roughness to adhesive dissipation. In Figs. 14a

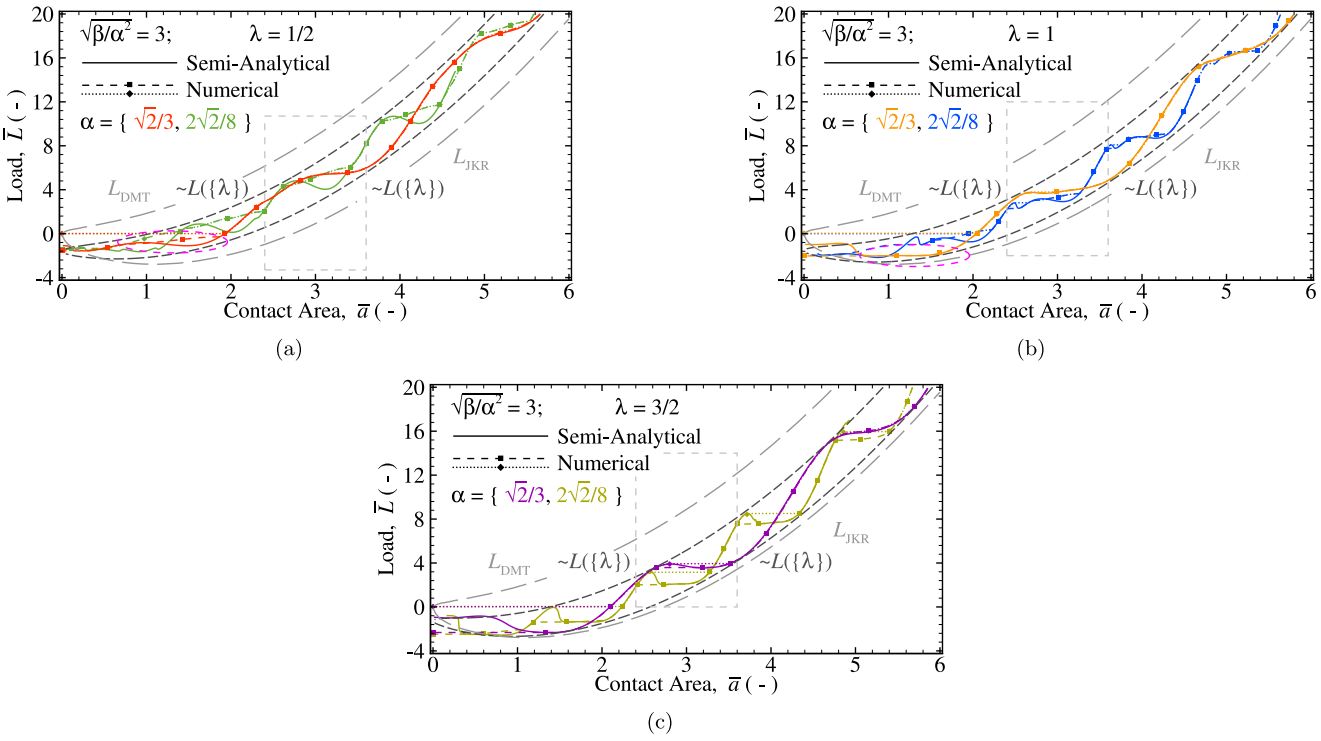

Fig. 13. Normalised load $\bar{L}$ as a function of the contact area $\bar{a}$ for wave parameters $\{\alpha,\beta\}=\{\sqrt{2}/3,2\}$ and $\{2\sqrt{2}/8,9/8\}$, with Maugis parameter (a) $\lambda=1/2$, (b) 1 and (c) 3/2. The medium-dashed, dark grey lines indicate the local envelope (17) as a function of Maugis parameter λ, and the long, dashed lines the JKR (E.42b) and (M-)DMT (E.43d) envelope.

and b, the load-area response is presented again for Maugis parameters $\lambda=1/2$, 1 and 3/2, with wave parameters $\{\alpha,\beta\}=\left\{\sqrt{2}/3,2\right\}$ and $\left\{2\sqrt{2}/8,9/8\right\}$, respectively, for a restricted range of intimate contact area $2.4\leq\bar{a}\leq3.6$; the results of wave parameters $\{\alpha,\beta\}=\left\{\sqrt{2}/3,2\right\}$ and $\left\{2\sqrt{2}/8,9/8\right\}$ are shown in Figs. 14a and b, respectively; the plot range of each load-area trajectory is indicated with light grey, dashed rectangles in Fig. 13; the load $\bar{L}$ is translated along the vertical axis by a constant $C(\{2\lambda=1\})=2.3$, $C(\{\lambda=1\})=1$ and $C(\{2\lambda=3\})=-1$ for clarity sake. In Figs. 14c and d, the numerical substrate $u(x)$ and traction profile $p(x)$ are given for the Maugis parameters $\lambda=1/2$ and 1 with roughness parameters $\{\alpha,\beta\}=\left\{\sqrt{2}/3,2\right\}$ and $\left\{2\sqrt{2}/8,9/8\right\}$ for the intimate contact area $\bar{a}=3$; the loci with the intimate contact areas $\bar{a}\approx3$ are indicated with coloured, Delta-shaped markers in Figs. 14a and b. The result for Maugis parameter $\lambda=3/2$ in Figs. 14a and b is not shown in c and d because no stable quasi-static contact is attained at intimate contact area $\bar{a}=3$.

For the largest given amplitude $\alpha=\sqrt{2}/3$ and longest wavelength $\beta=2$, the intimate contact area is continuous in Figs. 14a and c; for the smallest given amplitude $\alpha=2\sqrt{2}/8$ and shortest wavelength $\beta=9/8$, the semi-analytical and numerical results no longer coincide in Fig. 14b and the contact cavitates via adhesive strips in d. For Maugis parameter $\lambda=3/2$, we observe that mechanical instabilities occur both during loading and unloading. With Maugis parameters $\lambda=1$ and 1/2 for roughness parameters $\{\alpha,\beta\}=\left\{\sqrt{2}/3,2\right\}$ the intimate contact area remains continuous. This observation corresponds with the traction profiles in Fig. 14c. For Maugis parameter $\lambda\leq1$, the intimate contact cavitates at the valleys of the wavy profile, that border the outermost crests in intimate contact in Fig. 14d. We find notable that mechanical instabilities and cavitation do occur successively for a particular range of Maugis parameter (herein $\lambda=1$ with wave parameters $\{\alpha,\beta\}=\left\{2\sqrt{2}/8,9/8\right\}$). This confirms that mechanical instability and cavitation are mutually exclusive at a given load-area locus but not across the whole load-area trajectory. Note that during instabilities cavities might appear and then disappear, yet our numerical method does not provide for this, because it solves for stable quasi-static equilibrium. Once the Maugis parameter is small enough, here with $\lambda\leq1/2$, the substrate no longer conforms to the wave roughness and mechanical instabilities are absent.

For the given scaled Johnson parameter $\sqrt{\beta/\alpha^2}=3$ all three regimes are observed in Fig. 14; the Johnson parameter alone does not uniquely capture adhesive dissipation. Inspecting the load-area trajectory with total intimate contact area $\bar{a}<2$ and Maugis parameters $\lambda=1/2$ and 1, we find that the intimate contact area cavitates for roughness parameter $\{\alpha,\beta\}=\left\{\sqrt{2}/3,2\right\}$ with a decreasing Maugis parameter as well. The sections of the load-area curves we considered here are marked with dashed, pink coloured ellipses in Figs. 13a and b. Connectivity of the intimate contact area thus also depends on the locus of the load-area curve one considers.

The numerically obtained deformations outside of contact in Figs. 14c and d differ little between normalised amplitudes $\alpha=\sqrt{2}/3$ and $2\sqrt{2}/8$, respectively, for the intimate contact area $\bar{a}\approx3$ with the given Maugis parameters $\lambda=1$ and 1/2. Hence the Maugis parameter λ for which the adhesive behaviour during retraction changes from continuous to fragmented intimate contact mainly depends on dimensionless wave traction $\alpha/(\beta\lambda)=3/\left(9\sqrt{2}\lambda\right)$ and $4/\left(9\sqrt{2}\lambda\right)$ in Figs. 14a and c, and 14b and d, respectively. This argument suffices during both loading and unloading because cavitation prevents loading-unloading hysteresis and thus the need to consider the gap in the adhesive strips, $g(a<|x|\leq c)$, during loading. Hence the contact toughness depends on the inverse wave traction $\beta\lambda/\alpha$ (See Section 5.2 as well). Note that the dimensionless parameter $\beta\lambda/\alpha$ appears to control the occurrence of instability/cavitation with finite Maugis parameter λ yet is not a quantitative measure of roughness-induced dissipation.

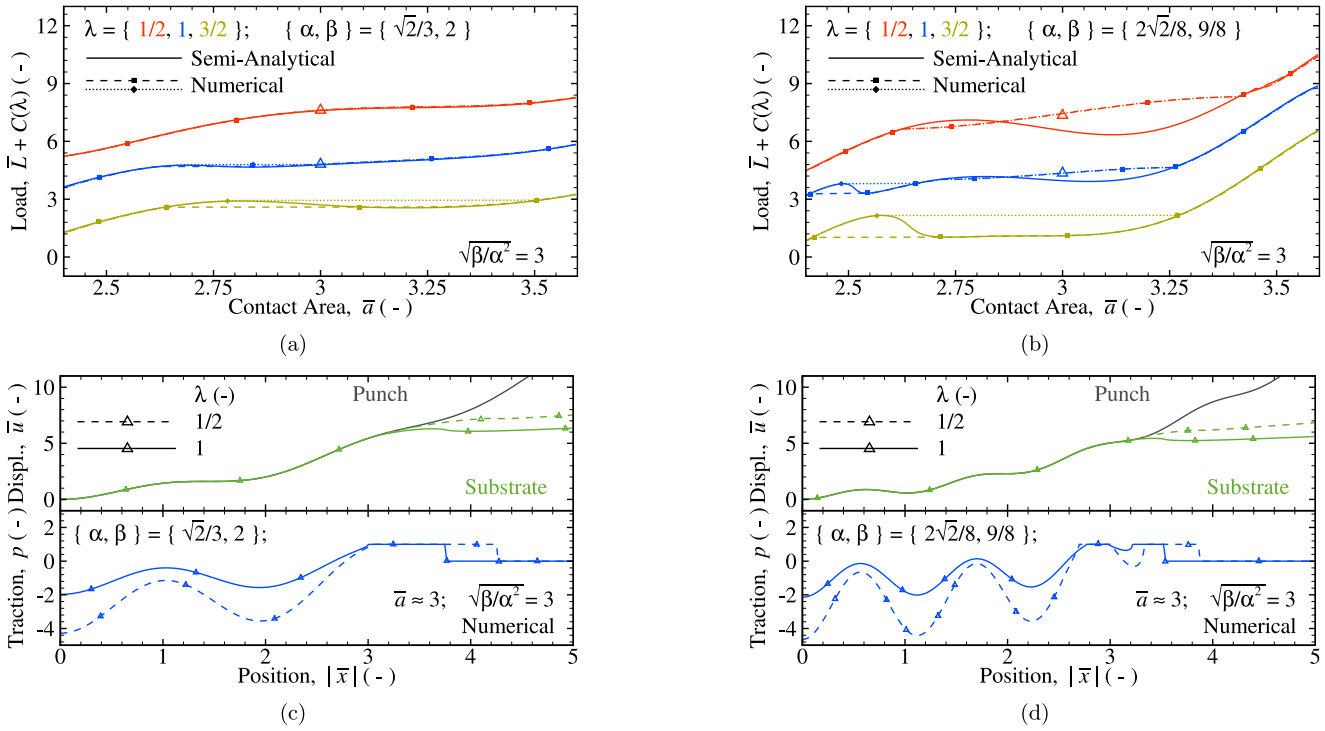

Fig. 14. (a,b) Normalised load $\bar{L}$ as a function of the intimate contact area $\bar{a}$ for Maugis parameters $\lambda = 1/2$, 1 and 3/2, with wave parameters (a) $\{\alpha, \beta\} = \left\{\sqrt{2}/3, 2\right\}$ and (b) $\left\{2\sqrt{2}/8, 9/8\right\}$. (c,d) The numerical normalised displacement $\bar{u}$ and normalised traction $\bar{p}$ as a function of the normalised position $|\bar{x}|$ with roughness parameters (c) $\{\alpha, \beta\} = \left\{2/\sqrt{3}, 2\right\}$ and (d) $\left\{2\sqrt{2}/8, 9/8\right\}$ for Maugis parameters $\lambda = 1/10$ and $1/2$. The intimate contact area (c,d) $\bar{a} \approx 3$ is indicated by Delta-shaped markers in (a,b).

To summarise, the Maugis parameter λ is the relative measure of the substrate elastic compliance scaled with the adhesive strength σ that accounts for the system size R/δ, *i.e.* the size-dependent contact compliance. The maximum positive traction inside of intimate contact is proportional to $\alpha/(\beta\lambda)$; the amplitude of the sinusoidal expansion of the integral on the RHS of the adhesive traction (16) is of order $\alpha/(\beta\lambda)$ when the wavelength $\beta \ll \bar{a}$. The maximum adhesive traction necessary to maintain intimate contact at valleys thus increases with decreasing Maugis parameter λ. Hence, for a given Maugis parameter, the contact toughens with instabilities for decreasing wave roughness; the contact weakens via cavitation and increasing wave roughness. Here, (interface) toughness is used synonymously with the additional work necessary to form or break intimate contact compared to smooth contact (Guduru and Bull, 2007; Guduru, 2007; Waters et al., 2009). Furthermore, the chance of cavitation increases with normalised amplitude α and decreases with normalised wavelength β. The gap outside of intimate contact $g(a < |x|)$ decreases with Maugis parameter λ, while the size of the adhesive strips $|c - a|$ increases. Hereby the chance of crests adjacent to intimate contact to come into compressive contact during loading increase. Instability at high Maugis parameter λ or adhesive strips $a < |x| \leq c$ that encompass a valley and a crest are not prerequisite for cavitation with decreasing λ. Hence contact cavitates because with decreasing Maugis parameter $\lambda = 1/2 \cdots 1/10$, the contact stiffens, all before a semi-analytical mechanical instability can occur. Mechanical instability and cavitation thus appear mutually exclusive at a given load-area locus.

We observe the following three, adhesive response regimes: continuous intimate contact without mechanical instabilities; continuous intimate contact with mechanical instabilities; and, cavitation. In the JKR-limit $\lambda \sim \infty$, the substrate conforms to the wave roughness inside contact. Energy is then dissipated when a mechanical instability occurs between two stable, static equilibria (See Section 5.1). We agree with Guduru (2007) that for a sufficient initial load and finite roughness, continuous (intimate) contact is maintained during retraction. Intimate contact solely cavitates when the wave traction $p(|x| < a)$ surpasses the traction $\Delta\gamma/\delta$ (See Section 5.2). In the JKR-limit the interaction range vanishes, *i.e.* $\delta \sim 0$, and adhesive traction $\sigma \sim \infty$. Hence the (intimate) contact area remains continuous during retraction for any finite, wave roughness because cavitation is prevented. The contact mechanical response depends on applied load for high, yet finite, Maugis parameters, which is in agreement with the statement by Guduru (2007) and previous works (Zhu et al., 2021; Pérez-Ràfols et al., 2023). Notable is that there is a minimum amplitude α and maximum wavelength β for Maugis parameters $1 \ll \lambda$, below and above which, respectively, no roughness-induced dissipation is observed either (See Fig. 4a with roughness parameters $\{\alpha, \beta\} = \left\{2\sqrt{2}/8, 2\right\}$ and Maugis parameter $\lambda = 3$). When the Maugis parameter λ decreases the contact stiffness increases whereby the substrate still conforms to the wavy profile but the difference in intimate contact area Δa between static equilibria becomes loading direction dependent. With Maugis parameters $1/2 \leq \lambda < 3/2$, continuous contact with and without mechanical instabilities, and cavitation are observed. Finally, when one reduces the Maugis parameter even further, with $\lambda < 1$, solely continuous contact without mechanical instabilities and/or cavitation is observed. With vanishing Maugis parameter $\lambda \ll 1/2$, intimate contact must cavitate because no tensile traction is sustained at wave valleys in intimate contact as the substrate stiffens. The successive adhesive response regimes we find with decreasing contact compliance thus are: continuous contact without mechanical instabilities then only cavitation; continuous contact with mechanical instabilities and/or cavitation, then solely cavitation; and, not presented herein, cavitation with high wave parameters.

6. Concluding remarks

In this work, we perform the Maugis analysis of the adhesive line contact between a cylinder with various wave profiles and an elastic, semi-infinite half-plane. We show that the adhesive contact mechanics depends on the Maugis parameter as a measure of the size-dependent contact compliance, and on the profile geometry: the amplitude and the wavelength. Whether the Johnson parameter is a measure of the envelope that encloses the load-area response for small Maugis parameters is hitherto unknown. We find that the maximum envelope of the load-area response is captured by the Johnson parameter, where smooth adhesionless and JKR contact give the maximum and minimum bound of the load-area response. However, the Johnson parameter does not uniquely determine roughness-induced dissipation for a finite Maugis parameter as the amplitude (or wavelength) is also necessary.

With a given wave profile and a decreasing Maugis parameter, the adhesive response changes from a load-area trajectory with discontinuous, mechanical jumps in intimate contact area to a continuous decrease of the total contact area. For moderate Maugis parameters, equivalent maximum traction inside and adhesive traction outside of intimate contact, and the simultaneous increase in the range of adhesion allow for smaller intimate contact areas during unloading than JKR. For sufficiently low Maugis parameters, cavities under tensile traction inside of contact appear because the wavy substrate becomes too stiff for a continuous intimate contact. Adhesive dissipation thus decreases when there is an increase in the range of adhesion and the adhesive traction decreases. Similarly, contact toughness vanishes above a critical wave roughness. Notable is that during indentation and retraction both mechanical jumps and cavitation can occur. While mechanical instabilities and cavitation are mutually exclusive they thus do coexist at different loci on the given load-area curve. Intimate contact does remain continuous though for low Maugis parameters and sufficiently low wave roughness, and for high Maugis parameters and a sufficiently high (maximum) load. These findings are obviously limited to cylindrical indenters with single scale roughness.

In macro- and mesoscopic adhesive contacts the Maugis parameter is typically large enough that our semi-analytical analysis is valid in the presence of microscale roughness. Recent experiments show that rough Hertzian contact predominantly peels at the edge of contact (Lyashenko and Pohrt, 2020), *i.e.* without cavitation. Furthermore, our analysis is useful in the model interpretation of soft matter contact where adhesion and viscoelasticity act simultaneously, and the intimate contact area might remain continuous (Pérez-Ràfols et al., 2023). For sufficiently high roughness amplitudes and short-enough wavelengths, the chance of cavitation increases though. The Maugis analysis then allows interpenetration inside of the adhesive strips, which limits the range of validity of our semi-analytical solution, and advanced analysis (Zhu et al., 2021) is necessary. The exact functional dependence of the transitional value of the Maugis parameter and load hysteresis, for which contact cavitates, remains unknown, hence a good starting point for future work.

CRediT authorship contribution statement

Jan Steven Van Dokkum: Writing – review & editing, Writing – original draft, Visualization, Validation, Software, Methodology, Investigation, Formal analysis, Conceptualization. **Francesc Pérez-Ràfols:** Writing – review & editing, Supervision, Software, Investigation. **Lucia Nicola:** Writing – review & editing, Supervision, Investigation, Funding acquisition.

Declaration of competing interest

The authors declare that they have no known competing financial interests or personal relationships that could have appeared to influence the work reported in this paper.

Data availability

Data will be made available on request.

Acknowledgements

The authors would like to hereby thank A. Sanner for proof reading the original manuscript. One of the authors (LN) acknowledges funding from the European Research Council (ERC) under the European Union's Horizon 2020 research and innovation programme (grant agreement no. 681813).

Appendix A. Symmetric adhesive line contact

Adhesive contact corresponds with the (singular) JKR-theory by Johnson et al. (1971) when the interaction range vanishes, *i.e.* $\delta \sim 0$, and the adhesive traction

$$p^{\mathrm{a}}_{\mathrm{JKR}}(x) = \frac{L^{\mathrm{JKR}}_{\mathrm{a}}}{\pi\sqrt{a^2 - x^2}}, \tag{A.1a}$$

for $|x| \leq a$, where $L^{\mathrm{JKR}}_{\mathrm{a}} = -\sqrt{2\pi E^* \Delta\gamma a}$ is the adhesive contribution to the total load $L(a)$, which ensures that the energy release rate $\left(K^{\mathrm{JKR}}_{\mathrm{I}\pm a}\right)^2/E^*$ is equal to the work of adhesion $\Delta\gamma$, with the Mode I stress intensity factor,

$$K^{\mathrm{JKR}}_{\mathrm{I}\pm a} \equiv \lim_{x\to a^-} p^{\mathrm{a}}_{\mathrm{JKR}}(x)\sqrt{2\pi(x-a)} = \frac{L^{\mathrm{JKR}}_{\mathrm{a}}}{\sqrt{\pi a}}. \tag{A.1b}$$

The adhesive traction (A.1a) with generic load $L^{\mathrm{JKR}}_{\mathrm{a}} = L'_{\mathrm{a}}(a)$ leads to a uniform deformation within the contact area, that is zero at the edges of adhesionless contact (Johnson and Johnson, 1987). The total traction that results in zero external load (Baney and Hui, 1997) when one applies the Dugdale-Maugis traction (Dugdale, 1960; Maugis, 2000) to an external crack under plane strain condition is given by Tada et al. (1973):

$$p^{\mathrm{a}}_{\mathrm{Dugdale}}(x) = \tag{A.2}$$
$$\begin{cases} \dfrac{2\sigma}{\pi}\left(\tan^{-1}\left(\sqrt{\dfrac{c^2-a^2}{a^2-x^2}}\right) - \sqrt{\dfrac{c^2-a^2}{a^2-x^2}}\right), & |x| \leq a \quad ; \\ \sigma, & a < |x| \leq c \quad ; \\ 0, & c < |x| \quad ; \end{cases}.$$

The condition that governs the cancellation of stress singularities at $|x| = a$ is expressed as

$$K^{\mathrm{Dugdale}}_{\mathrm{I}\pm a} \equiv K^{\mathrm{JKR}}_{\mathrm{I}\pm a}, \tag{A.3a}$$

with stress intensities:

$$K^{\mathrm{Dugdale}}_{\mathrm{I}\pm a} = \frac{2\sigma}{\sqrt{\pi a}}\sqrt{c^2 - a^2}; \quad \text{and,} \quad K^{\mathrm{JKR}}_{\mathrm{I}\pm a} = \frac{L'_{\mathrm{a}}(a)}{\sqrt{\pi a}}, \tag{A.3b}$$

where $K^{\mathrm{Dugdale}}_{\mathrm{I}\pm a}$ is the Mode I stress intensity factor when loading external cracks with a constant traction σ in an infinite elastic solid under plane stain condition (Maugis, 2000), and $K^{\mathrm{JKR}}_{\mathrm{I}\pm a}$ the Mode I stress intensity factor of said external cracks under a far-field load $L'_{\mathrm{a}}(a)$, which is not necessarily equal to the adhesive load $L^{\mathrm{JKR}}_{\mathrm{a}}$. Using Eqs. (A.3), we give the adhesive traction inside of the intimate contact area due to the far-field load $L'_{\mathrm{a}}(a)$ as

$$p^{\mathrm{a}}_{L'_{\mathrm{a}}}(x) = \frac{2\sigma}{\pi}\frac{\sqrt{c^2 - a^2}}{\sqrt{a^2 - x^2}}, \tag{A.4a}$$

and via Eq. (A.3), find the total adhesive traction

$$p^{\mathrm{a}}(x) \equiv p^{\mathrm{a}}_{\mathrm{Dugdale}}(x) + p^{\mathrm{a}}_{L'_{\mathrm{a}}}(x) = \tag{A.4b}$$

$$u_{\mathrm{a}}(x) = \frac{4\sigma}{\pi E^*}\begin{cases} 0, & |x| \le a\ ; \\ c\cosh^{-1}\!\left(\frac{|x|}{a}\sqrt{\frac{c^2-a^2}{c^2-x^2}}\right) - |x|\cosh^{-1}\!\left(\sqrt{\frac{c^2-a^2}{c^2-x^2}}\right) - \sqrt{c^2-a^2}\cosh^{-1}\!\left(\frac{|x|}{a}\right), & a<|x|<c\ ; \\ c\sinh^{-1}\!\left(\frac{|x|}{a}\sqrt{\frac{c^2-a^2}{x^2-c^2}}\right) - |x|\sinh^{-1}\!\left(\sqrt{\frac{c^2-a^2}{x^2-c^2}}\right) - \sqrt{c^2-a^2}\cosh^{-1}\!\left(\frac{|x|}{a}\right), & c\le|x| \quad ; \end{cases} \tag{A.5a}$$

Box I.

$$\begin{cases} \frac{2\sigma}{\pi}\tan^{-1}\!\left(\sqrt{\frac{c^2-a^2}{a^2-x^2}}\right), & |x| \le a\ ; \\ \sigma, & a<|x|\le c\ ; \\ 0, & c<|x|\ ; \end{cases};$$

and, the adhesive load,

$$L_{\mathrm{a}}^{\mathrm{M}}(a) \equiv -\int_{-\infty}^{\infty} p^{\mathrm{a}}(x)\,\mathrm{d}x = -2\sigma\sqrt{c^2-a^2}. \tag{A.4c}$$

The displacement due to adhesion in symmetric, line contact (Johnson and Greenwood, 2008) is reproduced in Box I and the displacement at the edge of the adhesive strips:

$$u_{\mathrm{a}}(|x|=c) = \frac{4\sigma}{\pi E^*}c\ln\!\left(\frac{c}{a}\right) - \frac{4\sigma}{\pi E^*}\sqrt{c^2-a^2}\cosh^{-1}\!\left(\frac{c}{a}\right), \tag{A.5b}$$

where the first term on the RHS is due to the adhesive traction σ over the adhesive strips $|c-a|$ (Tada et al., 1973) and the second term on the RHS due to a far-field load $L'_{\mathrm{a}} \equiv L_{\mathrm{a}}^{\mathrm{M}}$ (Baney and Hui, 1997; Johnson and Greenwood, 2008).

Appendix B. Wavy surface contact in plane strain

Substituting the surface gradient (5a) in Eq. (6), we find the Fourier coefficients of the adhesionless traction

$$p_0^{\mathrm{c}} = -\frac{L_{\mathrm{c}}(a)}{\pi a}, \tag{B.6a}$$

with the middle term of Eq. (B.13); and,

$$p_n^{\mathrm{c}} = \frac{E^* f_n}{2a}, \quad \text{for,} \quad 1 \le n. \tag{B.6b}$$

We note here the difference of the factor half between Eq. (B.6b) and the expression (54) on page 367 in Guduru (2007), which both depend on the type of discrete Fourier transform. Taking the derivative of the profile (1) and using the change of variables (5c), we rewrite the profile gradient as

$$\frac{a^2}{2R}\sin(2\phi) + \frac{2\pi Aa}{\zeta}\sin(\phi)\sin\!\left(\frac{2\pi a}{\zeta}\cos(\phi)\right) = \sum_{n=1}^{\infty} f_n \sin(n\phi)\,. \tag{B.7}$$

Multiplying the gradient (B.7) with $\sin(m\phi)$ and integration over $-\pi \le \phi \le \pi$, using the identity (Abramowitz et al., 1988):

$$\int_{-\pi}^{\pi}\sin(nt)\sin(mt)\,\mathrm{d}t = \begin{cases} 0, & \text{for, } n \ne m; \\ \pi, & \text{for, } n = m; \end{cases}, \tag{B.8}$$

we give the Fourier coefficients of the gradient of the profile, at positions $|x| < a$, by

$$f_0 = f_1 = 0; \qquad f_2 = \frac{a^2}{2R} + \frac{2Aa}{\zeta}\int_{-\pi}^{\pi}\sin(\phi)\sin(2\phi)\sin\!\left(\frac{2\pi a}{\zeta}\cos(\phi)\right)\mathrm{d}\phi;$$

$$f_m = \frac{2Aa}{\zeta}\int_{-\pi}^{\pi}\sin(\phi)\sin(m\phi)\sin\!\left(\frac{2\pi a}{\zeta}\cos(\phi)\right)\mathrm{d}\phi, \qquad \text{for,} \quad 2 < m \in 2\mathbb{Z};$$

$$\text{else,} \qquad f_m = 0. \tag{B.9a}$$

Here, $\mathbb{Z}$ indicates the set of real-valued integers. The integral representation of the Bessel function of order k' (Abramowitz et al., 1988):

$$\mathrm{J}_{k'}(z) = \frac{1}{\pi}\int_0^{\pi}\cos\!\big(k'\theta - z\sin(\theta)\big)\,\mathrm{d}\theta, \tag{B.10}$$

with the complex-valued scalar z. The prime $\bullet'$ is used to distinguish between indices $\bullet$. Using the integral representation of the Bessel function of order k' (B.10), we rewrite the Fourier coefficient of the adhesionless traction (B.6) as

$$p_0^{\mathrm{c}} = -\frac{L_{\mathrm{c}}(a)}{\pi a}; \qquad p_1^{\mathrm{c}} = 0; \qquad p_2^{\mathrm{c}} = \frac{E^* a}{4R} + \frac{2E^* A}{a}\mathrm{J}_2\!\left(\frac{2\pi a}{\zeta}\right);$$

$$\text{and,} \quad p_m^{\mathrm{c}} = \frac{E^* A}{2a}\mathrm{i}^{m+2}\left(1+\mathrm{i}^{2m}\right) m\,\mathrm{J}_m\!\left(\frac{2\pi a}{\zeta}\right), \quad \text{for} \quad 2 < m, \tag{B.11}$$

where $\mathrm{i} \equiv \sqrt{-1}$ is the imaginary number. Combining the definition of the Fourier transform of the traction (5b) and its coefficients (B.11), we obtain the adhesionless traction as

$$p^{\mathrm{c}}(\theta) = -\frac{L_{\mathrm{c}}(a)}{\pi a\sin(\theta)} + \frac{E^* a\cos(2\theta)}{4R\sin(\theta)} + \frac{2E^* A}{a\sin(\theta)}\sum_{n=1}^{\infty}(-1)^{n+1} n\,\mathrm{J}_{2n}\!\left(\frac{2\pi a}{\zeta}\right)\cos(2n\theta)\,. \tag{B.12}$$

Note that in this equation (B.12) the integer n is no longer the wavenumber but an index. The adhesionless load (Guduru, 2007):

$$L_{\mathrm{c}}(a) \equiv L_{\mathrm{H}}(a) + L_{\mathrm{w}}(a) = -\int_{-a}^{a} p^{\mathrm{c}}(x)\,\mathrm{d}x = \frac{\pi E^* a^2}{4R} + \frac{\pi^2 E^* Aa}{\zeta}\mathrm{J}_1\!\left(\frac{2\pi a}{\zeta}\right), \tag{B.13}$$

with the Hertzian load, $L_{\mathrm{H}}(a)$, and the load provided by the waviness of the cylinder profile, $L_{\mathrm{w}}(a)$, where $J_{k'}(\bullet)$, with scalar $\bullet$, is the (ordinary) Bessel function (B.10) of order k'. Using the adhesionless load (B.13) and the summation (Abramowitz et al., 1988):

$$\sum_{n=1}^{\infty}(-1)^n n\,\mathrm{J}_{2n}\!\left(\frac{2\pi a}{\zeta}\right) = -\frac{\pi a}{2\zeta}\mathrm{J}_1\!\left(\frac{2\pi a}{\zeta}\right), \tag{B.14}$$

we rewrite the adhesionless traction (B.12) as

$$p^{\mathrm{c}}(\theta) = -\frac{E^* a\sin(\theta)}{2R} - \frac{\pi E^* A}{\zeta\sin(\theta)}\mathrm{J}_1\!\left(\frac{2\pi a}{\zeta}\right)\cdots \tag{B.15}$$

$$\cdots - \frac{2E^* A}{a\sin(\theta)}\sum_{n=1}^{\infty}(-1)^n n\,\mathrm{J}_{2n}\!\left(\frac{2\pi a}{\zeta}\right)\cos(2n\theta)\,.$$

Using the recurrence relationship (Abramowitz et al., 1988):

$$\mathrm{J}_{m+1}(z) = \frac{2\,m}{z}\mathrm{J}_m(z) - \mathrm{J}_{m-1}(z), \tag{B.16}$$

we rewrite the series on the RHS of Eq. (B.15) as

$$\sum_{n=1}^{\infty}(-1)^n n\,\mathrm{J}_{2n}(D)\cos(2n\theta) = \tag{B.17}$$

$$\frac{1}{4}\sum_{n=1}^{\infty}(-1)^n D\,\mathrm{J}_{2n-1}(D)\cos(2n\theta) + \frac{1}{4}\sum_{n=1}^{\infty}(-1)^n D\,\mathrm{J}_{2n+1}(D)\cos(2n\theta)\,,$$

with a scalar $D \equiv 2\pi a/\zeta$. Using the angle addition and subtraction theorem, we expand the infinite series on the RHS of (B.17) into four infinite series as

$$4\sum_{n=1}^{\infty}(-1)^n n\,\mathrm{J}_{2n}(D)\cos(2n\theta) = \tag{B.18}$$

$$\frac{D}{\cos(\theta)}\sum_{n=1}^{\infty}(-1)^n \mathrm{J}_{2n-1}(D)\cos\big((2n-1)\theta\big) - \frac{D\sin(\theta)}{\cos(\theta)}\sum_{n=1}^{\infty}(-1)^n J_{2n-1}(D)\sin(2n\theta)$$

$$+\frac{D}{\sin(\theta)}\sum_{n=1}^{\infty}(-1)^n \mathrm{J}_{2n+1}(D)\sin\big((2n+1)\theta\big)$$
$$-\frac{D\cos(\theta)}{\sin(\theta)}\sum_{n=1}^{\infty}(-1)^n J_{2n+1}(D)\sin(2n\theta).$$

The expansion of the Schwarz function into series of Bessel functions (Luke, 2014):

$$\int_0^z e^{-\mathrm{i}t\cos(\theta)}\mathrm{J}_v(t)\,\mathrm{d}t = \frac{2e^{-\mathrm{i}z\cos(\theta)}}{\sin(\theta)}\sum_{k=0}^{\infty}\mathrm{i}^k \mathrm{J}_{k+v+1}(z)\sin\big((1+k)\,\theta\big), \tag{B.19}$$

for $\Re(v) > -1$, where $\Re(\bullet)$ the real part of the complex scalar $\bullet$. We rewrite the expansion of the Schwarz function (B.19) in its even (*i.e.* real valued) terms as

$$\frac{2D}{\sin(\theta)}\sum_{k=0}^{\infty}(-1)^n \mathrm{J}_{2n+1}(D)\sin\big((2n+1)\theta\big) = \int_0^D \mathrm{J}_0(t)\cos\big((t-D)\cos(\theta)\big)\,\mathrm{d}t; \tag{B.20}$$

and, the generating function (Abramowitz et al., 1988):

$$2\sum_{n=0}^{\infty}(-1)^n \mathrm{J}_{2n+1}(z)\cos\big((2n+1)\theta\big) = \sin\big(z\cos(\theta)\big). \tag{B.21}$$

Using Eqs. (B.18), (B.20) and (B.21), the angle addition and subtraction theorem and well-known properties of the Bessel function (Abramowitz et al., 1988), we obtain the definite integral

$$\sum_{n=1}^{\infty}(-1)^n n\,\mathrm{J}_{2n}\left(\frac{2a\pi}{\zeta}\right)\cos(2n\theta) = \tag{B.22}$$
$$-\frac{\pi a}{2\zeta}\mathrm{J}_1\left(\frac{2\pi a}{\zeta}\right) + \frac{\pi a\sin^2(\theta)}{2\zeta}\int_0^{\frac{2\pi a}{\zeta}} J_0(t)\cos\left(\left(t-\frac{2\pi a}{\zeta}\right)\cos(\theta)\right)\mathrm{d}t.$$

Substituting the definite integral (B.22) in Eq. (B.15), we obtain the adhesionless traction (7). Using the convolution type integral (Abramowitz et al., 1988):

$$\int_0^z \frac{\mathrm{J}_k(t)\,\mathrm{J}_v(z-t)}{t}\,\mathrm{d}t = \frac{\mathrm{J}_{k+v}(z)}{k}, \tag{B.23}$$

with $\Re(k) > 0$; and $\Re(v) > -1$, we obtain the adhesionless load (B.13) by Guduru (2007) as well.

Appendix C. Substrate deformation gradient

For the integration of trigonometric convolutions with multiple poles we use a change of variables:

$$w = e^{\mathrm{i}\phi}; \qquad z = e^{\mathrm{i}\theta}; \qquad \text{and,} \qquad \mathrm{d}\theta = \mathrm{d}z/(\mathrm{i}z)\,. \tag{C.24}$$

where $\mathrm{i} \equiv \sqrt{-1}$ is the imaginary number. Subsequently, using the residue theorem, we find the convolution integral as the sum of residues in the unit disk, on the complex plane, when the spatial coordinate $a < |x|$,

$$I = \sum_l \mathrm{Res}(z_l)\,, \tag{C.25}$$

with the residues of the complex function $\mathrm{Res}(z_l)$ at poles $|z_l| < 1$.

C.1. Hertzian deformation gradient

The Hertzian deformation gradient

$$\frac{\partial}{\partial x}u_{\mathrm{H}}(x) = \frac{a}{R\cos(\phi)} + \frac{a}{2\pi R}\int_0^{2\pi}\frac{\tan^2(\phi)}{\cos(\theta)-\frac{1}{\cos(\phi)}}\,\mathrm{d}\theta, \tag{C.26}$$

with the angle $0 \le \phi < \pi/2$. Using the change of variables (C.24), we rewrite the integral on the RHS of Eq. (C.26) as

$$I_{\mathrm{H}} = 2\mathrm{i}\oint_{|z|=1}\frac{\left(w^2-1\right)^2}{\left(w^2+1\right)\left(w^2z^2+z^2-4wz+w^2+1\right)}\,\mathrm{d}z. \tag{C.27}$$

The simple poles are

$$z_1 = \frac{2w+\sqrt{-w^4+2w^2-1}}{w^2+1}; \text{ and, } z_2 = \frac{2w-\sqrt{-w^4+2w^2-1}}{w^2+1}. \tag{C.28}$$

Using Eqs. (C.24), (C.25) and (C.28), we find the integral in Eq. (C.26) as

$$I_{\mathrm{H}} = 2\pi\mathrm{i}\,\mathrm{Res}(z_2) = -2\pi\tan(\phi). \tag{C.29}$$

C.2. Wave deformation gradient

We rewrite the inner integral of Eq. (11a) as

$$I_{\mathrm{w}} = \tag{C.30}$$
$$\frac{1}{\mathrm{i}}\oint_{|z|=1}\frac{\left(w^2+1\right)\left(z^2-1\right)^2}{4z^2\left(w^2z^2+z^2-4wz+w^2+1\right)}\left(e^{-\frac{1}{2}\mathrm{i}B\left(z+\frac{1}{z}\right)}+e^{\frac{1}{2}\mathrm{i}B\left(z+\frac{1}{z}\right)}\right)\mathrm{d}z,$$

with a scalar $B \equiv t - 2\pi a/\zeta$. The simple poles are given by Eq. (C.28) and the double pole $z_3 = 0$. The residual of this simple pole

$$\mathrm{Res}(z_2) = \frac{\sqrt{a^2-x^2}}{a}\cos\left(\frac{Bx}{a}\right). \tag{C.31}$$

For the double pole at $z_3 = 0$, we use the infinitive series (Abramowitz et al., 1988):

$$e^z = \sum_{k'=0}^{\infty}\frac{z^{k'}}{k'!}, \tag{C.32}$$

that we substitute into the integrand in Eq. (C.30), which we give as

$$\frac{1}{4\mathrm{i}}\frac{\left(w^2+1\right)\left(z^2-1\right)^2}{\left(w^2z^2+z^2-4wz+w^2+1\right)z^2}\left(\sum_{k'=0}^{\infty}\frac{1}{k'!}\left(\frac{B}{2\mathrm{i}}\left(z+\frac{1}{z}\right)\right)^{k'}\cdots\right.$$
$$\left.\cdots+\sum_{k'=0}^{\infty}\frac{1}{k'!}\left(\frac{\mathrm{i}B}{2}\left(z+\frac{1}{z}\right)\right)^{k'}\right). \tag{C.33}$$

Taking the Taylor series expansion of Eq. (C.33) around zero, collecting the coefficients of z^{-1} and multiplying them by $2\pi\mathrm{i}$, we find the residue of the $k' = 0,\ldots,8$ non-zero terms

$$2\pi\mathrm{i}\,\mathrm{Res}(z_3) \approx \tag{C.34a}$$
$$\frac{2\pi x}{a}+\frac{\pi x}{2a^3}\left(a^2-2x^2\right)B^2-\frac{\pi x}{96a^5}\left(a^4+4a^2x^2-8x^4\right)B^4\cdots$$
$$\cdots+\frac{\pi x}{5760a^7}\left(a^6+2a^4x^2+8a^2x^4-16x^6\right)B^6\cdots$$
$$\cdots-\frac{\pi x}{2580480a^9}\left(5a^8+8a^6x^2+16a^4x^4+64a^2x^6-128x^8\right)B^8+\quad\ldots,$$

of the infinite series:

$$2\pi\mathrm{i}\,\mathrm{Res}(z_3) = \tag{C.34b}$$
$$-\frac{\pi x}{a}\sum_{k=0}^{\infty}\frac{(-1)^k}{\Gamma(1+2k)}\left(\frac{Bx}{a}\right)^{2k}\sum_{m'=0}^{k}\frac{\Gamma\left(m'-\frac{1}{2}\right)}{\sqrt{\pi}\Gamma(1+m')}\left(\frac{a}{z}\right)^{2m'},$$

where $\Gamma(\bullet)$ is the Gamma function of scalar $\bullet$. We rewrite the inner sum on the RHS of Eq. (C.34b) as

$$\sum_{m'=0}^{k}\frac{\Gamma\left(m'-\frac{1}{2}\right)}{\sqrt{\pi}\Gamma(1+m')}\left(\frac{a}{x}\right)^{2m'} = \tag{C.35a}$$
$$-\frac{\Gamma\left(\frac{1}{2}+k\right)}{\sqrt{\pi}}\left(\frac{a}{x}\right)^{2(k+1)}{}_2\mathrm{F}_1\left(1,k+\frac{1}{2};k+2;\left(\frac{a}{x}\right)^2\right)-2\sqrt{1-\left(\frac{a}{x}\right)^2},$$

with the hypergeometric function (Abramowitz et al., 1988):

$${}_2\mathrm{F}_1(\bullet_1,\bullet_2;\bullet_3;z) = \sum_{k'=0}^{\infty}\frac{\Gamma(\bullet_1+k')\Gamma(\bullet_2+k')\Gamma(\bullet_3)}{\Gamma(\bullet_1)\Gamma(\bullet_2)\Gamma(\bullet_3+k')}\frac{z^{k'}}{k'!}. \tag{C.35b}$$

Substituting the residues (C.31) and (C.34b) in Eq. (C.25), using the definition (C.35a), and noting that

$$\cos(z) = \sum_{k=0}^{\infty}\frac{(-1)^k}{\Gamma(2k+1)}z^{2k}, \tag{C.36}$$

we find the inner integral

$$I_{\mathrm{w}} = \frac{\pi a}{x}\sum_{k=0}^{\infty}\frac{(-1)^k}{\Gamma(k+1)\Gamma(k+2)}\left(\frac{B}{2}\right)^{2k}{}_2\mathrm{F}_1\left(1,k+\frac{1}{2};k+2;\left(\frac{a}{x}\right)^2\right). \tag{C.37}$$

Substituting Eq. (C.37) in Eq. (11a), we give the wave deformation gradient

$$\frac{\partial}{\partial x}u_{\mathrm{w}}(x) = \frac{\pi A a}{\zeta x}\sum_{k=0}^{\infty}\frac{(-1)^k}{\Gamma(1+k)\Gamma(2+k)2^{(2k)}}\cdots \tag{C.38}$$
$$\cdots\,{}_2\mathrm{F}_1\left(1,k+\frac{1}{2};k+2;\left(\frac{a}{x}\right)^2\right)\int_0^{\frac{2\pi a}{\zeta}}\mathrm{J}_0(t)\left(t-\frac{2\pi a}{\zeta}\right)^{2k}\mathrm{d}t.$$

We solve the integral on the RHS of Eq. (C.38) as

$$\int_0^{\frac{2\pi a}{\zeta}}\mathrm{J}_0(t)\left(t-\frac{2\pi a}{\zeta}\right)^{2k}\mathrm{d}t = \tag{C.39a}$$
$$\frac{2\pi a}{\zeta}\frac{1}{2k+1}\left(\frac{2\pi a}{\zeta}\right)^{2k}{}_1\mathrm{F}_2\left(\frac{1}{2};k+1,k+\frac{3}{2};-\left(\frac{\pi a}{\zeta}\right)^2\right),$$

with the generalised hypergeometric function (Abramowitz et al., 1988):

$${}_1\mathrm{F}_2(\bullet_1;\bullet_2,\bullet_3;z) = \sum_{k'=0}^{\infty}\frac{\Gamma(\bullet_1+k')\Gamma(\bullet_2)\Gamma(\bullet_3)}{\Gamma(\bullet_1)\Gamma(\bullet_2+k')\Gamma(\bullet_3+k')}\frac{z^{k'}}{k'!}. \tag{C.39b}$$

Appendix D. Wave deformation

Integrating the deformation gradient (11b), we give the wave deformation as

$$u_{\mathrm{w}}(x) = 2A\left(\frac{\pi a}{\lambda}\right)^2\sum_{k=0}^{\infty}\frac{1}{\Gamma(k+1)\Gamma(k+2)}\frac{(-1)^k}{(2k+1)}\left(-\frac{\pi a}{\lambda}\right)^{2k}\cdots \tag{D.40}$$
$$\cdots\,{}_1\mathrm{F}_2\left(\frac{1}{2};k+1,k+\frac{3}{2};-\left(\frac{\pi a}{\zeta}\right)^2\right)\int\left(\frac{1}{x}\right){}_2\mathrm{F}_1\left(1,k+\frac{1}{2};k+2;\left(\frac{a}{x}\right)^2\right)\mathrm{d}x.$$

We solve the integral on the RHS of Eq. (D.40) as

$$\int\left(\frac{1}{x}\right){}_2\mathrm{F}_1\left(1,k+\frac{1}{2};k+2;\left(\frac{a}{x}\right)^2\right)\mathrm{d}x = \tag{D.41a}$$
$$\frac{\Gamma(k+2)}{2\Gamma\left(k+\frac{1}{2}\right)}\mathrm{G}^{2,2}_{3,3}\left(-\left(\frac{a}{x}\right)^2\middle|\begin{matrix}0,\frac{1}{2}-k,1\\0,0,-k-1\end{matrix}\right),$$

with the Meijer-G function,

$$\mathrm{G}^{l,0}_{i,j}\left(z\middle|\begin{matrix}\bullet_1,\cdots,\bullet_i\\\bullet_1,\cdots,\bullet_j\end{matrix}\right), \tag{D.41b}$$

where $\bullet_{(i,j)}$ are scalars, and l and o integers (Abramowitz et al., 1988).

Appendix E. Load-area response limits

The well-known JKR-theory for Hertzian contact in the presence of waviness is given by Guduru (2007):

$$\bar{L}_{\mathrm{JKR}} = \frac{\pi\bar{a}^2}{4} + \frac{\pi^2\alpha\bar{a}}{\beta}\mathrm{J}_1\left(\frac{2\pi\bar{a}}{\beta}\right) - \sqrt{2\pi}\sqrt{\bar{a}}, \tag{E.42a}$$

which corresponds with the limit $\lambda \sim \infty$, and approaches $3 \leq \lambda$ in smooth contact (Johnson and Greenwood, 2008). Using the asymptotic expansion of the Bessel function for large arguments (Abramowitz et al., 1988), Kesari et al. (2010) give the JKR-envelope of the load-area response:

$$\bar{L}_{\mathrm{JKR}} \sim \frac{\pi\bar{a}^2}{4} \pm \pi\sqrt{\frac{\alpha^2}{\beta}}\sqrt{\bar{a}} - \sqrt{2\pi}\sqrt{\bar{a}}. \tag{E.42b}$$

The lower branch of the envelope (E.42b) can be thought of as the minimum load limit. Similarly, we use the postulate by Maugis (1992), *i.e.* the M-DMT theory as discussed by Greenwood (2022):

$$\bar{L}_{\mathrm{DMT}} \equiv \bar{L}_{\mathrm{c}} - \bar{L}'_{\mathrm{p}} = \frac{\pi\bar{a}^2}{4} + \frac{\pi^2\alpha\bar{a}}{\beta}\mathrm{J}_1\left(\frac{2\pi\bar{a}}{\beta}\right) - \bar{L}^{\mathrm{r}}_{\mathrm{p}}, \tag{E.43a}$$

where the adhesive load equals the pull-off load for a rigid substrate $\bar{L}^{\mathrm{r}}_{\mathrm{p}}$; and, corresponds with the limit $\lambda \sim 0$, and approaches $\lambda < 1/10$ in smooth contact (Johnson and Greenwood, 2008). Setting the gap at the edge of the adhesive contact (1) equal to the interaction range, *i.e.* $f(c) \equiv g(c) = \delta$, we give the adhesive strip as

$$1 = \frac{1}{2}\lambda(m\bar{a})^2 + 2\alpha\lambda\sin^2\left(\frac{\pi m\bar{a}}{\beta}\right), \tag{E.43b}$$

and using the middle expression in Eq. (A.4c), the pull-off load by

$$\bar{L}^{\mathrm{r}}_{\mathrm{p}} \equiv -\bar{L}_{\mathrm{a}} = 2\lambda m\bar{a}. \tag{E.43c}$$

In the presence of waviness, the size of the adhesive strip $m\bar{a}$ at pull-off is obtained numerically, because no closed-form analytical solution is found. We give the M-DMT envelope of the load-area curve as

$$\bar{L}_{\mathrm{DMT}} \sim \frac{\pi\bar{a}^2}{4} \pm \pi\sqrt{\frac{\alpha^2}{\beta}}\sqrt{\bar{a}} - \bar{L}^{\mathrm{r}}_{\mathrm{p}}. \tag{E.43d}$$

The upper branch of the envelope (E.43d) for Maugis parameter $\lambda \sim 0$ can be thought of as the maximum load limit. For smooth contact, *i.e.* wave parameters $\{\alpha,\beta\} = \{0,-\}$, substituting Eq. (E.43b) in Eq. (E.43c), we reformulate the M-DMT load

$$\bar{L}^{\mathrm{H}}_{\mathrm{DMT}} = \frac{\pi\bar{a}^2}{4} - 2\sqrt{2}\sqrt{\lambda}, \tag{E.44}$$

with the pull-off load $\bar{L}^{\mathrm{r}}_{\mathrm{p}} = 2\sqrt{2}\sqrt{\lambda}$ as presented by Johnson and Greenwood (2008). Comparing the envelopes of the JKR- and the M-DMT theory (E.42b) and (E.43d), respectively, we find these are equal in size and independent of the Maugis parameter $\lambda \sim 0$ and ∞. Moreover, the pull-off load vanishes in the limit $\lambda \sim 0$, which stands in stark contrast with the finite pull-off force for axi-symmetric contacts (Johnson et al., 1971; Maugis, 1992, 2000). This is notable because waviness is not necessarily present in the load-area response for all Maugis parameters and roughness parameters $0 < \alpha$ and $0 < \beta < \infty$ (Zhu et al., 2021). Note though that these observations are limited to continuous intimate contact, and the soft- and adhesionless limit.

References

Abramowitz, M., Stegun, I.A., Romer, R.H., 1988. Handbook of Mathematical Functions with Formulas, Graphs, and Mathematical Tables.

Attard, P., Parker, J.L., 1992. Deformation and adhesion of elastic bodies in contact. Phys. Rev. A 46, 7959.

Badler, D., Goltsberg, R., Ammar, A.A., Kasem, H., 2023. Experimental study of adhesion, friction, and peeling of biomimetic combined micro-mushroom and micro-spatulae textures. Tribol. Int. 186, 108609.

Baney, J., Hui, C.-Y., 1997. A cohesive zone model for the adhesion of cylinders. J. Adhes. Sci. Technol. 11, 393–406.

Barber, J.R., 2018. Contact mechanics, vol. 250, Springer.

Barenblatt, G.I., 1962. The mathematical theory of equilibrium cracks in brittle fracture. Adv. Appl. Mech. 7, 55–129.

Barthel, E., 1998. On the description of the adhesive contact of spheres with arbitrary interaction potentials. J. Colloid Interface Sci. 200, 7–18.

Bazrafshan, M.d., De Rooij, M., Valefi, M., Schipper, D., 2017. Numerical method for the adhesive normal contact analysis based on a Dugdale approximation. Tribol. Int. 112, 117–128.

Briggs, G., Briscoe, B., 1977. The effect of surface topography on the adhesion of elastic solids. J. Phys. D: Appl. Phys. 10, 2453.

Campaná, C., Müser, M.H., 2007. Contact mechanics of real vs. randomly rough surfaces: A Green's function molecular dynamics study. Europhys. Lett. 77, 38005.

Carbone, G., Pierro, E., 2012. The influence of the fractal dimension of rough surfaces on the adhesion of elastic materials. J. Adhes. Sci. Technol. 26, 2555–2570.

Chumak, K., 2016. Adhesive contact between solids with periodically grooved surfaces. Int. J. Solids Struct. 78, 70–76.

Chumak, K., Chizhik, S., Martynyak, R., 2014. Adhesion of two elastic conforming solids with a single interface gap. J. Adhes. Sci. Technol. 28, 1568–1578.

Ciavarella, M., 2016. On roughness-induced adhesion enhancement. J. Strain Anal. Eng. Des. 51, 473–481.

Creton, C., Leibler, L., 1996. How does tack depend on time of contact and contact pressure? J. Polym. Sci. B 34, 545–554.

Dalvi, S., et al., 2019. Linking energy loss in soft adhesion to surface roughness. Proc. Natl. Acad. Sci. 116, 25484–25490.

Dugdale, D.S., 1960. Yielding of steel sheets containing slits. J. Mech. Phys. Solids 8, 100–104.

Feng, J.Q., 2000. Contact behavior of spherical elastic particles: a computational study of particle adhesion and deformations. Colloids Surf. A 172, 175–198.
Frigo, M., Johnson, S.G., 2005. The design and implementation of FFTW3. Proc. IEEE 93, 216–231, Special issue on Program Generation, Optimization, and Platform Adaptation.
Greenwood, J., 1997. Adhesion of elastic spheres. Proc. R. Soc. Lond. Ser. A Math. Phys. Eng. Sci. 453, 1277–1297.
Greenwood, J., 2022. Derjaguin and the DMT theory: A farewell to DMT? Tribol. Lett. 70, 61.
Guduru, P., 2007. Detachment of a rigid solid from an elastic wavy surface: theory. J. Mech. Phys. Solids 55, 445–472.
Guduru, P., Bull, C., 2007. Detachment of a rigid solid from an elastic wavy surface: Experiments. J. Mech. Phys. Solids 55, 473–488.
Hwang, D., et al., 2023. Metamaterial adhesives for programmable adhesion through reverse crack propagation. Nature Mater. 1–9.
Inc., W.R., 2023. Mathematica. Version 13.3. https://www.wolfram.com/mathematica. Champaign, IL.
Jin, F., Guo, X., Wan, Q., 2016. Revisiting the Maugis–Dugdale adhesion model of elastic periodic wavy surfaces. J. Appl. Mech. 83, 101007.
Johnson, K., 1995. The adhesion of two elastic bodies with slightly wavy surfaces. Int. J. Solids Struct. 32, 423–430.
Johnson, K., Greenwood, J., 1997. An adhesion map for the contact of elastic spheres. J. Colloid Interface Sci. 192, 326–333.
Johnson, K., Greenwood, J., 2008. A maugis analysis of adhesive line contact. J. Phys. D: Appl. Phys. 41, 155315.
Johnson, K.L., Johnson, K.L., 1987. Contact Mechanics. Cambridge University Press.
Johnson, K.L., Kendall, K., Roberts, A.D., 1971. Surface energy and the contact of elastic solids. Proc. R. Soc. A 324, 301–313.
Kesari, H., Doll, J.C., Pruitt, B.L., Cai, W., Lew, A.J., 2010. Role of surface roughness in hysteresis during adhesive elastic contact. Philos. Mag. Philos. Mag. Lett. 90, 891–902.
Kesari, H., Lew, A.J., 2011. Effective macroscopic adhesive contact behavior induced by small surface roughness. J. Mech. Phys. Solids 59, 2488–2510.
Lennard-Jones, J.E., 1931. Cohesion. Proc. Phys. Soc. 43, 461.
Linghu, C., et al., 2023. Overcoming the adhesion paradox and switchability conflict on rough surfaces with shape-memory polymers. Proc. Natl. Acad. Sci. 120, e2221049120.
Luke, Y.L., 2014. Integrals of Bessel Functions. Courier Corporation.
Lyashenko, I.A., Pohrt, R., 2020. Adhesion between rigid indenter and soft rubber layer: Influence of roughness. Front. Mech. Eng. 6, 49.
Maugis, D., 1992. Adhesion of spheres: the JKR-DMT transition using a dugdale model. J. Colloid Interface Sci. 150, 243–269.
Maugis, D., 2000. Contact, Adhesion and Rupture of Elastic Solids, vol. 130, Springer Science & Business Media.
Medina, S., Dini, D., 2014. A numerical model for the deterministic analysis of adhesive rough contacts down to the nano-scale. Int. J. Solids Struct. 51, 2620–2632.
Müser, M.H., Nicola, L., 2022. Modeling the surface topography dependence of friction, adhesion, and contact compliance. MRS Bull. 47, 1221–1228.
Pérez-Ràfols, F., Van Dokkum, J.S., Nicola, L., 2023. On the interplay between roughness and viscoelasticity in adhesive hysteresis. J. Mech. Phys. Solids 170, 105079.
Persson, B.N., Scaraggi, M., 2014. Theory of adhesion: Role of surface roughness. J. Chem. Phys. 141.
Sanner, Antoine, Kumar, Nityanshu, Dhinojwala, Ali, Jacobs, Tevis DB, Pastewka, Lars, 2024. Why soft contacts are stickier when breaking than when making them. Science Advances 10 (10), eadl1277.
Sanner, A., Pastewka, L., 2022. Crack-front model for adhesion of soft elastic spheres with chemical heterogeneity. J. Mech. Phys. Solids 160, 104781.
She, H., Chaudhury, M.K., 2000. Estimation of adhesion hysteresis using rolling contact mechanics. Langmuir 16, 622–625.
She, H., Malotky, D., Chaudhury, M.K., 1998. Estimation of adhesion hysteresis at polymer/oxide interfaces using rolling contact mechanics. Langmuir 14, 3090–3100.
Sneddon, I.N., 1965. The relation between load and penetration in the axisymmetric Boussinesq problem for a punch of arbitrary profile. Int. J. Eng. Sci. 3, 47–57.
Störmer, C., 1912. Sur les trajectoires des corpuscules électrisés dans l'espace sous l'action du magnétisme terrestre, avec application aux aurores boréales. Le Radium 9, 395–399.
Tabor, D., 1977. Surface Forces and Surface Interactions. Elsevier, pp. 3–14.
Tada, H., Paris, P.C., Irwin, G.R., 1973. The Stress Analysis of Cracks. Handbook, vol. 34, Del Research Corporation.
Van Dokkum, J.S., Nicola, L., 2019. Green's function molecular dynamics including viscoelasticity. Modelling Simul. Mater. Sci. Eng. 27, 075006.
Wang, A., Müser, M.H., 2023. Is there more than one stickiness criterion? Friction 11, 1027–1039.
Waters, J., Lee, S., Guduru, P., 2009. Mechanics of axisymmetric wavy surface adhesion: JKR–DMT transition solution. Int. J. Solids Struct. 46, 1033–1042.
Zheng, Z., Yu, J., 2007. Using the dugdale approximation to match a specific interaction in the adhesive contact of elastic objects. J. Colloid Interface Sci. 310, 27–34.
Zhu, Y., Zheng, Z., Huang, C., Yu, J., 2022. Adhesion of graded elastic materials: A full self-consistent model and its application. J. Mech. Phys. Solids 169, 105078.
Zhu, Y., Zheng, Z., Zhang, Y., Wu, H., Yu, J., 2021. Adhesion of elastic wavy surfaces: Interface strengthening/weakening and mode transition mechanisms. J. Mech. Phys. Solids 151, 104402.